Università degli Studi di Padova
Facoltà di Ingegneria

Finito di scrivere il giorno October 9, 2013 utilizzando LaTeX 2ε

UNIVERSITÀ DEGLI STUDI DI PADOVA
FACOLTÀ DI INGEGNERIA

—

DIPARTIMENTO DI INGEGNERIA DELL'INFORMAZIONE

—

TESI DI LAUREA SPECIALISTICA IN BIOINGEGNERIA

TOWARD A IMAGED-BASED POPULATION APPROACH TO RETINAL BIOMARKERS

RELATORE: PROF. RUGGERI ALFREDO
CORRELATORE: PROF. TRUCCO MANUEL

LAUREANDO: ALESSANDRO DAZZI

ANNO ACCADEMICO 2012-2013

alla mammma e al papà...

"Solo tre cose non mentono mai: i bambini, gli ubriachi ed i leggings.. "

Da Vinci

Contents

List of Figures

Abstract

The analysis of retinal images plays a key role in the prevention and the diagnosis of many diseases. The aim of this study is to establish whether there is a link between blood vessel appearances in the eye and muscle loss with age (sarcopenia). Several parameters are estimated in order to investigate changes in the retinal blood properties and to look at biomarkers which may help us identify people at risk of sarcopenia. We develop an innovative population image-based approach to retinal biomarkers, based on the estimation of the distribution of retinal vessel diameters. A pilot study on a community of older people affected by sarcopenia is presented.

Introduction

Age related loss of skeletal muscle and strength, sarcopenia - from the Greek terms *sarx* for flesh and *penia* for loss - is a common cause of falls, frailty and disability in old age. Research into this muscle loss is limited because, at present, it can only be diagnosed when the condition is far advanced. The mechanisms underlying this loss of muscle in old age have been not well understood yet, but recently evidence points to a link between it and cardiovascular disease.

The analysis of the retinal images plays a key role in the prevention and the diagnosis of many diseases. Photographing the back of the eye (retinal photography) allows the blood vessels of the eye to be seen directly, and is a routine rapid and well established way of screening people with diabetes for eye complications. We think that muscle loss in old age may be the results of disease in blood vessels throughout the body. To date, no one have studied the relationship between muscle loss in old age and the appearance of blood vessels. Eye photography may well help us identify older people at early risk of sarcopenia. This would allow us to target therapy to those most likely to benefit.

We use novel fundus camera retinal image processing to explore the link between sarcopenia and cardiovascular disease. Several parameters are estimated in order to investigate changes in the retinal blood proprieties and to look for biomarkers which would provide us with a new, simple, inexpensive and non-invasive assessment for detecting people at risk of sarcopenia. We propose an innovative population image-based approach to retinal biomarkers, based on the estimation of the distribution of retinal vessel diameter. Moreover, we develop a new definition of a surrogate measurement for vessel generation, based on blood flow rate estimation.

Chapter 1 provides a background of the topic: clinical aspects of sarcopenia disease and the state of art of retinal image analysis are presented.

Capter 2 presents two algorithms that have been used in a section of the work, respectively for vessel diameters estimation and AV (arteries and veins) classification.

Chapter 3 proposes an algorithm for estimation of distribution of vessels diameters. It could represent the starting point towards a novel population image-based approach to retinal biomarkers and a pilot study on a community dwelling older people is presented.

Finally, in chapter 4, we propose a new definition of a surrogate measurement for vessel generation for which there is pour agreement in literature. An attempt of blood flow rate estimation from morphometric measurements is also presented.

Chapter 1

Background

1.1 Background

Sarcopenia - from the Greek terms *sarx* and *penia* "loss of flesh" - is defined as the age-related involuntary loss of skeletal muscle mass, strength and physical function. The etiology is believed to be multi-factorial and includes ageing, disease, inflammation, increased oxidative stress, reduced physical activity, malnutrition, hormone deficiencies, muscle structural changes, and motor unit remodeling [1]. Sarcopenia represents a common cause of falls, frailty and disability in old age and is also associated with complications of diabetes, including a increased risk of vascular disease, heart attacks, strokes, blindness, liver and kidney disease [2],[3]. Thus, this leads to an increased requirement for nursing home placements, home healthcare and hospital facilities.

Therefore, if at an individual level, disability leads to reduced quality of life, at the social level it leads to an increase in healthcare expenditures. The estimated direct healthcare cost attributable to sarcopenia in the United States in 2000 was $18.5 billion, which represented about 1.5% of total healthcare expenditures for that year [4]. Reducing the prevalence of sarcopenia by 10% would result in savings of $1.1 billion per year in U.S. healthcare costs. [4] Recent estimates indicate that approximately 45% of the older U.S. population is sarcopenic and that approximately 20% of the older U.S. population is functionally disabled [4]. These numbers will rise significantly in the next years due the ageing of the population and the economic costs of aged related diseases will escalate unless effective public health campaigns aimed at reducing the occurrence of sarcopenia are implemented. For this reason, preventions, treatments and early diagnoses are essential.

Research into muscle loss is limited because, at present, it can only be diagnosed when the condition is far advanced. Several diagnostic protocols have been developed

such as physical activity questionnaires, body composition analysis, anthropometric and blood pressure measurement, muscle strength measurement and muscle performance tests [1]. However, these approaches are costly and time-consuming. An alternative method could be a non-invasive assessment, who is low cost, easily interpreted and comfortable for patients. Medical imaging, based on the detection of imaging biomarkers as indicator of the progress of the disease, could be a valid approach. Specifically, sarcopenia could be diagnosed by a non-invasive retinal assessment since evidence has recently established a link between age-related disease and cardiovascular disease [3].

1.1.1 Retinal biomarker

Biomarkers are proxies for biological and pathological processes that can be measured objectively. They are clinically useful when the biomarker precedes the disease process, thus serving as a risk factor, or when the biomarker acts as a surrogate for tissue or fluid that is not obtainable practically. Biomarkers can be used in the diagnosis and management of disease, for example using markers of blood pressure, cholesterol, and body mass index to determine the risk for cardiovascular disease.

The retina is a unique site where the microcirculation can be imaged directly, providing an opportunity to study *in vivo* the structure and pathology of the human circulation and the possibility of detecting changes in the microvasculature relating to the development of cardiovascular disease. Histo-pathological studies have demonstrated that these retinal signs reflect vascular damage from ageing, hypertension and other processes. Retinal biomarkers have become a target in research, because they can assist in elucidating mechanisms of disease, determining the risk of disease and disease progression, and serve as outcome parameters for clinical studies. Retinal microvascular abnormalities seen on fundus photography are associated with diabetes, hypertension, stroke and cognitive impairment. Often, diagnostic focus is placed on structural features of the vasculature such as vessel width, branching angles, and vessel tortuosity. Retinal blood vessels have similar size and physiology to cerebral small vessels and may act as a surrogate marker to them. Abnormalities are often subtle and may be missed by visual observation or conventional retinal image inspection.

The ability to image the retina and develop techniques for analyzing the images is of great interest. As its function requires the retina to see the outside world, the involved ocular structures have to be optically transparent for image formation. Thus, with proper techniques, the retina is visible from the outside, making the retinal tissue, and thereby brain tissue of which represent the natural extension, accessible for imaging non-invasively. Because the retina's function makes it a highly metabolically active

tissue with a double blood supply, the retina also allows direct noninvasive observation of the circulation.

To date, just a few studies have studied the relationship between muscle loss in sarcopenia and the appearance of retinal blood vessels [5]: changes in the retinal circulatory properties, such as decreasing in the number of the vessels, narrowing of the walls and reduction of blood flow could be important factors. Emerging evidence suggests a link between cardiovascular disease and physical function (sarcopenia) in old age. Arterial stiffness is an established cardiovascular risk factor. Arterial stiffness increases with age [5] and greater arterial stiffness with age has been demonstrated at many sites, including the retinal microcirculation [6]. Arterial stiffness is associated with low thigh muscle mass [7] and poor leg function in older people, both in those with and without peripheral arterial disease. Retinal arterial narrowing is known to be associated with increased arterial stiffness. The mechanisms linking microcirculatory changes to macrocirculatory changes are not known but evidence shows that retinal microvascular changes can reflect increases in arterial stiffness independent of measured blood pressure and vascular risk factors [8],[9]. An age related increase in inflammatory markers is implicated in the disruption of the microvascular endothelium. This is reflected in an increased retinal arterial tortuosity and microvascular changes with age [5]. Sarcopenia is associated with an increase in inflammatory markers and with a reduction in capillary density in skeletal muscle [5]. It is therefore plausible that retinal microvasculature changes could be associated with sarcopenia. Thus, fundus images could prove very useful in detecting any retinal biomarkers for sarcopenia and also to identify older people at early risk of sarcopenia.

1.2 Fundus of the eye

Fundus photography documents the fundus of the eye, i.e. the interior surface of the eye, opposite the lens, and includes the retina, optic disc, macula and fovea. The retina is a layered tissue lining the interior of the eye that enables the conversion of incoming light into a neural signal that is suitable for further processing in the visual cortex of the brain. It consists of an outer pigmented layer, in contact with the choroid, and an inner nervous layer, close to the vitreous body. At the center of the posterior part of the retina is an oval, yellowish area, the *macula lutea*, which is the area of the retina for the most distinct vision. It has a central depression, the *fovea centralis*. The optic nerve leaves the retina about $3mm$ to the medial side of the macula lutea by the optic disc. The *optic disc* is slightly depressed at its center, where it is pierced by the central artery of the retina. At the optic disc is a complete absence of rods and cones so that it is insensitive to light and is referred to as the “blind spot” [10].

The only arterial blood supply to the inner retina is from the central retinal artery (CRA), that runs along the inferior margin of the optic nerve sheath and enters the eye at the level of the optic nerve head. Within the optic nerve, the artery divides to form the inferior/superior nasal and temporal arteries, which supply the four quadrants of the retina. The retinal venous branches are distributed in a similar fashion, where the central retinal vein (CRV) is equivalent of the central retinal artery [11].

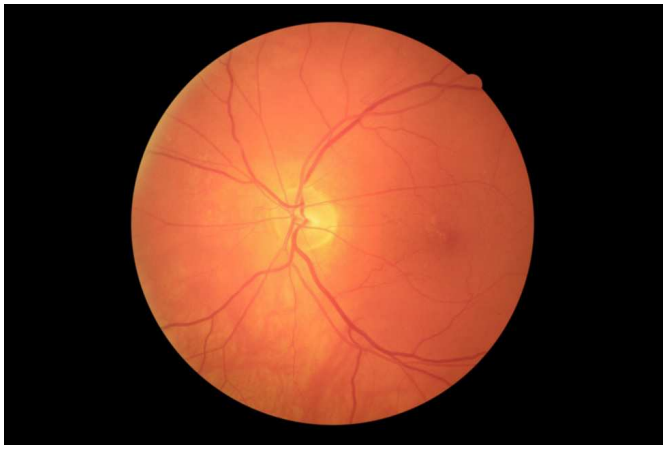

Figure 1.1: The left ocular fundus as seen with an ophthalmoscope. The image is centred on the optic disc.

1.3 Fundal Digital Image Analysis

The first stage in fundal digital image analysis is image capture. This is normally acquired by a fundal camera (mydriatic or non-mydriatic), that basically is a specialized low power microscope with an attached camera. The digital camera operates in the same fashion as a conventional camera, but instead of having film, they use a digital sensor (CCD, C-MOS) [12]. The CCD is an array of tiny light-sensitive diodes which convert the light signal (photons) into electrical charge (electrons). At each element in the array, the electrical current proportional to the analogue light level is converted into a digital level. Depending on the clinical application, various optical filters are available, the most common being green filters for red-free photography, and barrier filters for fluorescein angiography. A typical camera has a field of view (FOV) of 30 to 50° with a magnification of 2.5×. The actual image resolution, i.e., how many millimetres are captured by a pixel, depends on various factors, mainly the properties of the optics and the resolution of the CMOS/CCD image sensor employed. About 3000 × 3000 pixels are now common [13].

Nevertheless, taking manual measurements in retinal fundus images is time-consuming

Figure 1.2: A Canon CR-DGi fundus digital camera

and laborious, slowing down significantly the analysis of large numbers of images. Hence the need for software tools that can process large numbers of images in an objective, effective and efficient manner. Recent technologic advances in high resolution digital photography and image processing software programs have enabled quantitative and reproducible measurement of various changes in the retinal vasculature. Fundus imaging software also integrate visual information with reports, patient information and other data, and are designed to help ophthalmologists organize their efforts in an efficient and high-throughput manner. Retinal analysis systems usually follow the same schemes and implement the following steps:

- pre-processing: in order to obtain an image enhancement - contrast enhancement, denoising and correction of non-uniform illumination
- vascular net segmentation: the main step of every fundus images software
- landmark location: i.e. optic disc (OD) and fovea
- features extraction - e.g. vessel width, vessel tortuosity, branching coefficients, thickness
- lesion detection - e.g. automated detection of diabetic retinopathy (ADDR), microaneurysms and haemorrhages.

In the next section we present VAMPIRE [14], [15], a software for semi-automatic

quantification of retinal vessel properties, developed at the University of Dundee by the CVIP group. This discussion will also allow to have a general overview on the main features characterizing retinal fundus images and the some of the algorithms for their extraction.

1.3.1 VAMPIRE software for fundus retinal images analysis

VAMPIRE (Vascular Assessment and Measurement Platform for Images of the REtina) is an easy-to-use tool allowing efficient quantification of features of the retinal vasculature with hundreds or thousands of images. Most processing is performed automatically before user intervention, which is kept at a minimum. The VAMPIRE interface provides easy-to-understand visual feedback of the features extracted and a set of tools that allows the user to easily identify, locate and correct wrong measurements. No experience of image processing algorithms is assumed.

VAMPIRE starts with a segmentation of blood vessels and optic disc, followed by geometry estimation at vessel bifurcations, the tortuosity of major vessels, and fractal dimension of the vasculature. Most of the processing is hidden from the user, who is expected to provide only a minimal level of intervention after all measures are calculated. The current, beta version of VAMPIRE includes modules for vessel detection, branching angle measurements, vessel width estimation and tortuosity estimation. Optic disc location and fractal analysis are available and to be incorporated.

User interface: VAMPIRE allows the user to load a set of images of arbitrary size. At the moment, no automatic quality assessment is included. VAMPIRE locates the vasculature network and estimates branching coefficients, vessel widths, and tortuosity. The user can revise results efficiently, making corrections or discarding images. All measures, together with metadata about the images, are saved by VAMPIRE in Excel files, ready for analysis.

To date, VAMPIRE has been run for tests and pilot correlational studies on images of resolution ranging from approximately 400×400 to 3000×3000 pixels, acquired by various commercial instruments. These include fundus cameras (e.g. Canon CR-DGi nonmydriatic at about 45° FOV), and a scanning laser ophthalmoscope (henceforth SLO), the OPTOS P200 ultra-wide-field-of-view. VAMPIRE was run also on the main public datasets or retinal images, DRIVE, STARE and DIARETDB1.

Landmark location: the purpose is to locate key retinal landmarks, namely the optic disc (OD) and the fovea, and the approximate path of the arcade vessels. The de-

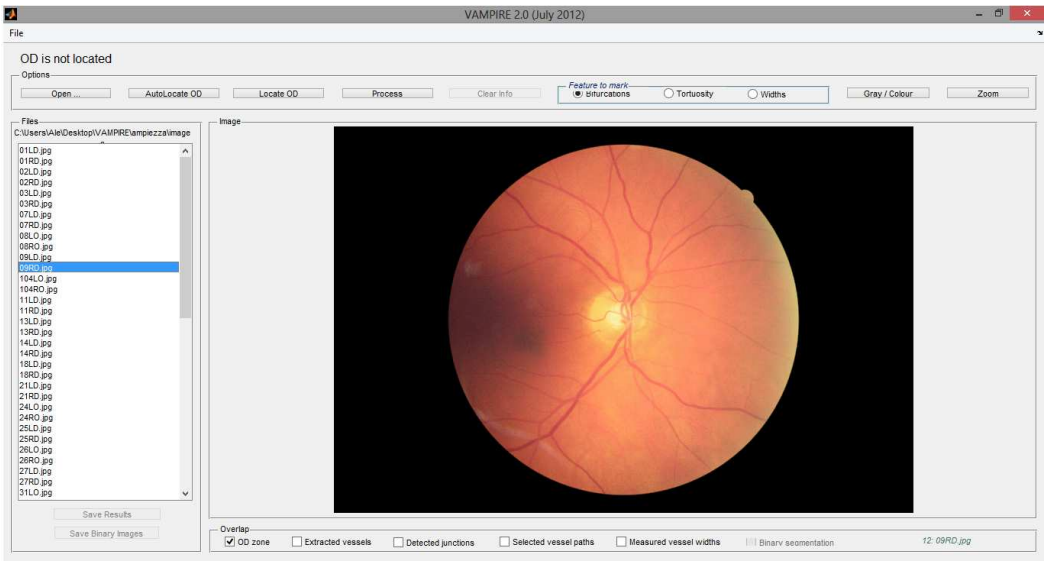

Figure 1.3: VAMPIRE interface

tectors exploit bright-dark circularly symmetric structures in vessel-removed, inpainted monochrome images and the method exploits the fact that the OD is crossed by large vessels, and the fovea located in an avascular zone.

The input image is converted to greyscale. Vessels are removed using the inpainting procedure described in [16]. Dark or bright radial symmetries are captured by the Fast Radial Symmetry transform by Loy and Zelinsky [17]. For each radius R in a defined range and for each pixel location $\vec{p}$, a positively affected pixel p_+ and a negative affected pixel p_- are obtained translating $\vec{p}$ along the gradient direction in positive (dark to bright) and negative (bright to dark) orientations. Values of the bright (OD) and dark (fovea) symmetry maps are generated by accumulating in "'affected"' pixels values depending on the gradient magnitude of the originating points and filtering maps in order to make the contribution scale invariant, and summing the contributions of all the radii used. If radii are densely sampled, the transform captures well all the symmetric structures in the range used. For OD detection the "positive" symmetry map S^+ on all integer radius values within 7 and 12 pixels in a subsampled image is computed. For the macular region the "negative" symmetry map S^- in the range 3-12 pixels is computed.

Vasculature detection: in order to locate and represent the retinal vessel network, trials with various vessel segmentation algorithms, including Soares et al. [18] and Lupascu et al. [19], were conducted. Currently, VAMPIRE implements a version of Soares's algorithm as the best compromise between speed and accuracy. In essence,

the algorithm applies a multi-scale, 2-D Gabor wavelet transforms to emphasize the appearance of vessels, followed by supervised pixel classification with a Bayesian classifier. Manually segmented images provide a labelled training set with two pixel classes, vessel and non-vessel. The authors report high accuracy (fraction of correctly classified pixels, 0.9466 and 0.9480 on DRIVE and STARE respectively). VAMPIRE implements this algorithm to generate a tree-like representation of the vasculature, as a pre-processing for measurements.

Vessel width: vessel contours in the binary maps are refined by a constrained spline-fitting algorithm [20], who allows a very good accuracy in width estimation on public dataset. First, a temporary skeleton is obtained using morphological thinning on the binary mask; branching points are removed and a natural cubic spline is fitted to the thinned centreline. Second, two coupled cubic splines are fitted to the original (jagged) contours by solving a linear system over-constrained by a parallel-tangent constraint coupling the two splines and penalizing locally non-parallel contours.

Vessel width w_j at point C_j lying on the spline smoothed centreline is estimated computing the Euclidean distance between points D_j and E_j on the two refined contours and lying on segment dj_j, orthogonal to the centreline at C_j.

Vessel tortuosity: the purpose is to define and assess the degree of tortuosity of selected retinal vessels. Currently, VAMPIRE adopt a new tortuosity metric that takes into account both skeleton curvature as well as vessel thickness [21]. The intuition is that at parity of skeleton, the curvature of the vessels boundaries changes width thickness: the measure is computed as the sum of the averaged curvatures od airs of corresponding boudary points. At the moment, only vessel segments between junctions are measured; estimates of the tortuosity of the whole vessel network are under study.

Branching coefficents: the goal is to quantify bifurcation geometry via branching angles and coefficients. Vessel center-lines are created from the binary vessel map and intersecting junction points of the three converging vessels are found for each junction. Following, three best-fit straight lines, one per vessel, are used to find the optimal junction location. A second set of lines crossing the estimated location are now fitted to vessel points. Results are used to estimate junction angles. The bifurcation coefficient, b, is determined from the widths of parent, W, and that of the two child vessels, $w1$, $w2$, as: $b = w_1^2 + w_2^2/W^2$.

Fractal analysis: the fractal dimension (FD) characterizes complex, repeating geometrical patterns at different spatial scales. In our case, FD measures the degree of

branching complexity of the vasculature tree. MFA is performed using the generalized sand-box method. This selects a random set of pixels and counts the number of vessel pixels in square regions centred at the selected pixels and with increasing linear dimension.

1.4 Numerical Simulation of Blood Flow

The computing of hemodynamic proprieties, i.e. pressure and flow profiles, could be very useful tool to diagnose arterial or venous disease. E.g. the challenge of ophthalmology management in patients with diabetes is the earliest detectable abnormalities in microvascular hemodynamics before gross morphologic changes appear. In this way the physician can intervene before complications arise and the effects of the disease become irreversible. Therefore, being able to construct a model based on measured geometry will allow to quantitatively understand the hemodynamics in a realistic retinal vascular network. For a given subject, measured pathologic flow profiles could be compared with computed healthy flow profiles. Studies of how the model parameters must change to simulate the measured pathologic flow profiles might lead to a better understanding of the pathologic condition.

Flow estimation from morphologic features Murray's law, based on the simple assumption of a steady Poiseuille blood flow, is usually used. It links the radius of a parent vessel R_0 (immediately upstream from a vessel bifurcation) to the radii of the daughter vessels R_1 and R_2 (immediately downstream after a vessel bifurcation) as $R_0/R_1 = R_0/R_2 = 2^{-1/3}$. From Murray's analysis, the required condition of minimum power occurs when $Q \propto R^3$ where Q denotes the volumetric flow. This relation, called "cube law", is determined assuming that two energy terms contribute to the cost of maintaining blood flow in any section of any vessel: (i) the pumping power and (ii) the energy metabolically required to maintain the volume of blood which is referred to as "volume constraint". A generalization of this relation can be proposed as $Q \propto R^c$ where c is determined from the condition of minimum power by assuming other constraints (for instance surface constraint yields $Q \propto R^{2.5}$). Under the condition $c = 3$, the shear stress on the vessel walls is uniform and independent of vessel diameter. Several studies have been carried out to determine the value of c which usually ranges between 2 and 3. In their article [22], Riva et al. present quantitative measurements of blood velocity and volumetric flow rate in individual arteries and veins of the normal human retina and establish their relation to vessel diameter. They found that volumetric flow rate varied with D (vessel diameter) at a power of 2.76 ± 0.16 for arteries and 2.84 ± 0.12 for veins, in close agreement with Murray's law. Exactly, fitting data points of 64 arteries and 66 veins, they found that Q_a varies as $2.0 \times 10^{-5} \times D^{2.76}$ and Q_v as $8.25 \times -10^{-6} \times D^{2.84}$

where D is in micron-meter.

Many authors developed mathematical models of hemodynamic proprieties of microcvascular retinal network. In their paper [23], Takahashi and Nagaoka et. al. develop a theoretical concept to quantitatively describe hemodynamic behaviour in the microvascular network of the human retina: a dichotomous symmetric branching network of the retinal vasculature was constructed, based on a combination of Murray's law and a mathematical model of fractal vascular trees. In [24] blood flow in the large systemic arteries was modeled using 1D equations derived from the axisymmetric Navier-Stokes equations for flow in compliant and tapering vessels. J. Malek et al. [25] developed a detailed 2D computational model to simulate blood flow in a realistic retinal arterial tree by solving Navier-Stokes equations and CFD analysis allowed them to examine the effect of topological changes in retinal vasculature on hemodynamics distribution in the retinal circulation.

In addition, the model of a microvascular network, such as the retina microcirculation, is further complicated by the dependence of blood viscosity from several parameters, vessel diameter, shear rate and hematocrit and these effects has to be taken into account. E.g. Pries et al. [26] developed a theoretical model to simulate blood flow through large microcirculatory networks: the model takes into account the dependence of apparent viscosity of blood on vessel diameter and hematocrit (the Fahraeus Lindqvist effect), the reduction of intravascular hematocrit relative to the inflow hematocrit of a vessel (the Fahraeus effect), and the disproportionate distribution of red blood cells and plasma at arteriolar bifurcations (phase separation).

Chapter 2

Related Works

In this chapter we reported 2 algorithms, respectively for automatic vessel diameter estimation and AV classification, that were of service of this project.

2.1 Width estimation

Reported algorithms estimating the diameter of retinal vessels in fundus camera images follow two broad schemes. The first is to fit a parametric model of the image intensity profile across the vessel, then estimate width from the best-fit parametric profile. The second is to use contour detection methods to find vessel boundaries directly. In this section, we present an algorithm of the former type, developed by Lupascu et. al. [27], who basically uses a novel parametric surface to model the local cross-sectional intensities and a ensembles of bagged decision trees for regression to estimate width from the parameters of the best-fit surface.

The algorithm consist of three main steps: the extraction of 3d intensity surface, the fitting of the surface with an extended multiresolution Hermite model and the width estimation by of the parameter of the fitting with ensembles of bagged decision trees. The next paragraphs briefly summarize the three sections, but for more details you can see [27].

2.1.1 Extraction of 3D surface

The surface of image intensities around a selected location is obtained from the green channel. The target location is automatically detected as the point of minimum intensity within the cross-sectional profile and 5 parallel cross-section on each side of the target location (for a total of 11 points) are set as seeds poins for the extraction profile. For each of the 11 seed points, you get the intensity profiles perpendicular to the vessel, using bilinear interpolation of intensities at non-integer locations. The length of

the profiles, fixed to a value large enough to contain the widest vessel cross-section, is taken to be 100 pixels Figure 2.1.

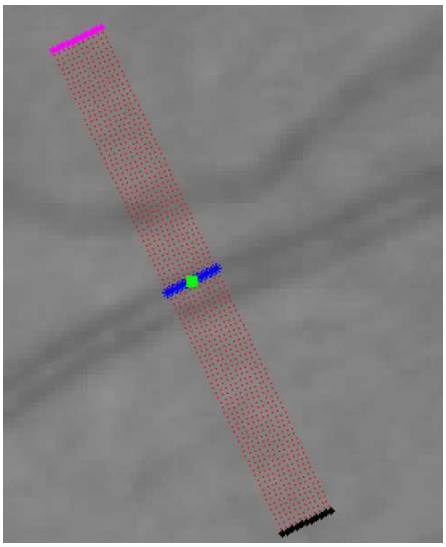

Figure 2.1: Seed points (blue asterisks), profile points (red circles), profile borders (magenta and black diamonds) and automatic target location (green square).

The next step is to identify vessel region around target location on the mean intensity profile in order to cut intensity profile regions of other vessels profiles. To automatically obtain the vessel region, the local maxima and minima need to be detected. Specific rules to group maxima and relate them to different vessels have been established; they can captured both vessel with and without central reflex.

2.1.2 Extended multiresolution Hermite model

Intensity cross-section profiles of retinal vessels are approximately Gaussian in shape, but not infrequently large vessels present a central light reflex caused by specular reflection. In this case a Gaussian intensity model tends to over-segment the features, consequently underestimating width.

The starting point is the model suggest by Wang et. al. [28], who uses a second-order Hermite polynomial to modulate a Gaussian, and shows to fit very well the intensity profile of retinal vessels, thanks to its ability to represent the possible central reflex of some vessels. However, Wang model cannot get all vessel proprieties, e.g. it can't explain for the asymmetric profile of some vessel, so some parameters with specific functions were introduced in order to improve the fitting to the vessel surface. Here we report the final expression of the extension of multiresolution Hermite model:

$$H(a, m, \delta, \sigma, p, q, x, y) = p[1 + a((x - m - \delta)^2 - 1)]\frac{1}{\sqrt{2\pi\delta^2}}e^{\frac{-(x-m)^2}{2\delta^2}} + q \tag{2.1}$$

where:

- a: asses the central deformation of the Gaussian
- m: the mean of the Gaussian
- σ: the standar deviation of the Gaussian
- δ: accounts for the asymmetric profiles
- p: allows to change the sign of the function
- q: shifts the function along y-axis, ensuring positive values.

The fitting of the surface is achieved by the a Nelder-Mead optimizer, minimizing the sum of squared differences between model and intensity data. To initialize the optimization, the mean profile over the 11 cross-sections is computed and used its maximum and minimum peaks to obtain the parameter values of a 1D, subsequently pushed out to obtain the initialization of the surface.

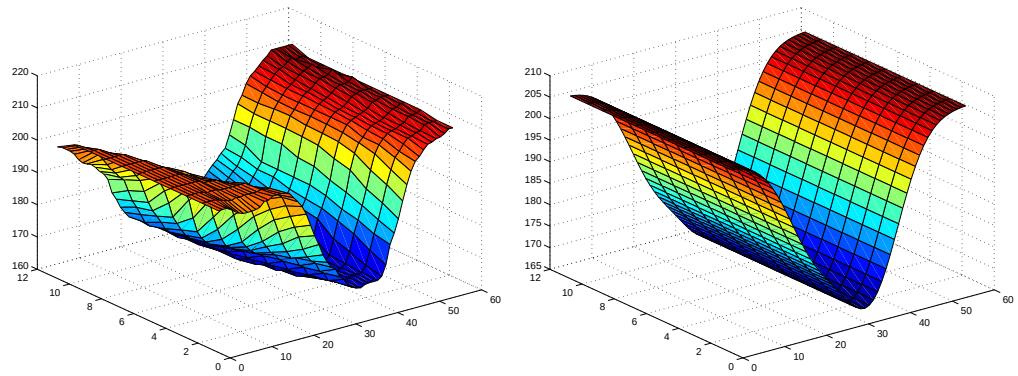

(a) (b)

Figure 2.2: Vessel intensity profile before (a) and after fitting (b).

2.1.3 Width estimation

The final step is to associate the parameters of the best-fit intensity surface with a width value. To do this, they use ensembles of bagged decision trees to learn the mapping from a point in the 6d parameter space, representing the surface, to the vessel diameter.

2.1.4 Results

The classifier was trained on 378 cross-sections of main and secondary vessels, estimated manually by 2 clinicians. The dataset includes and belonging to 38 healthy and diseased images, resolution 2336×3504, from the Tayside diabetic retinopathy screening

programme, obtained in full conformity with the current protocols (ethics, Caldicott, anonymization) training. 10-fold cross validation was performed in order to assess the accuracy of the classifier and test on public dataset and compared their method width other algorithms proposed in literature. The classification error is expressed as mean and standard deviation of the difference between the estimated value and the ground truth, computed on all the profiles available; results show good accuracy (the error ranges from 0.004 ± 0.438 to 0.015 ± 1.073, depends on the dataset) and better success rate (100%).

2.2 AV classification

In the retinal vasculature it is essential to classify vessels in artery and veins, due to the possibility of extracting diagnostic indicators, as the Arteriolar to Venular ratio (AVR), that has been linked to different disease. For this reason several authors [29], [30] proposed methods to discriminate veins and arteries on retinal images. The classification problem can be faced both with supervised and unsupervised approaches. In this section we present an algorithms of the second type, who focuses on the selection on a large number of optimal features and test different supervised classifications methods; for major details you can see [31].

2.2.1 Features Extraction

They considered a large number of features, for a total of 86 features, including not only color features, but also spatial location and vessel size. They can be summarize as follows:

- colour: the main features are related to colour inside the vessels. Both colour variations within in the vessel and contrast with the surrounding pixels were computed: central pixel colour components (RGB, HSV), components derivatives, mean, minimum, maximum and standard deviation of these values.
- position and size: vessel size and spatial location can be used together and in combination of colour features to improve the classification accuracy: they decided to computed polar coordinates (angle and distance from OD).

2.2.2 Vessels labelling

They performed supervised classification and feature selection tests based on the computation of the parameters described in the previous section, using the PRTools Matlab toolkit [32]. They tested different linear and non-linear classifiers (Linear and Quadratic Normal Bayes, Parzen Classifier, Linear and radial basis Support Vector Machine), using different subset of features.

2.2.3 Results

They performed tests on a database of 42 images acquired within the Tayside diabetic screening programme at Ninewells Hospital, Dundee, in accordance to the current regulations (ethics, Caldicott, anonymization). Images have high resolution (2336×3504), and type-2 field, i.e., centered on the macula. Images were also subsampled by different factors (0.625, 0.5, 0.25, 0.125, 0.0625) in order to simulate acquisition with sensor with different resolutions and tests have been repeated at each obtained resolution.

The best classification accuracy was obtained with the normal linear Bayes classifier (classification error 0.06875) using subsets of features described above and considering color variations within the vessel size or also outside. It's worth to highlight some interesting facts:

- colour variations are more informative considering both vessel and background than using vessel only. Contrast with external pixels give more information than internal variability (central reflex), even if the addition of features based on the internal variations slightly improve the results
- size information alone does not improve the colour based classification accuracy, while positional information does relevantly reduce the classification error
- the classification results and the role of feature groups does change with the resolution and that the accuracy does not necessarily decrease with it: indeed, it is maximal at about half the original size (0.625)
- vessel size is one of the best features and that a lot of colour features are relevant for the classification.

Chapter 3

Estimation of distribution of vessel widths

In this section we present a method for the estimation of the distribution of arteriolar and venular widths in a set of retinal fundus images. The double purpose is to introduce a new approach of investigation of vessel widths based on images and to characterize a community dwelling older people with maps of distribution of retinal vessel diameters. This study will allow us to characterize a populations of sarcopenic patients in order to establish if there is any significant change in retinal vasculature compared to healthy subjects.

3.1 Material

We used a set of 150 field-1 retinal images (N=75, left and right-eye images for each), 2304×3456 pixel, of older people (> 65 years, mean age 72 ± 6) volunteers from a recent study on retinal biomarkers for Sarcopenia [5]. Participants with inability to walk independently, past medical history of diabetes mellitus, stroke (within 6 months) and significant visual impairment were excluded from the study. Images were taken at the diabetes screening centre at Ninewells Hospital, Dundee, with a non-mydriatic digital camera after dilation of the pupils with 1% tropicamide eye drops. 13 participants had sarcopenia, 14 had pre-sarcopenia, no one had severe sarcopenia.

3.2 Methods

The algorithm is divided in three main parts: the estimation of the vessel diameter in the set of images, registration of the images and the interpolation of the collected data. They are described in details in the next sections.

3.2.1 Data collection

For each image, widths were computed automatically at N=600 locations taken on concentric circles of different diameters d_i, centred on the OD. A location on a circle is defined as a point where a vessel skeleton crosses the circle and it is detected automatically by an operation of binary intersection of two sets, respectively the skeleton of the binary map of retinal vasculature and a binary circular mask (Figure 3.1b). The number of locations per circle thus varies. The algorithm starts with 5 circles ($r = 1, 2, \ldots, 5$ OD radius) and adds inbetween circles until the target total number of measurements is reached. This guarantees a regular sampling of the vasculature, with about 30 circles per image.

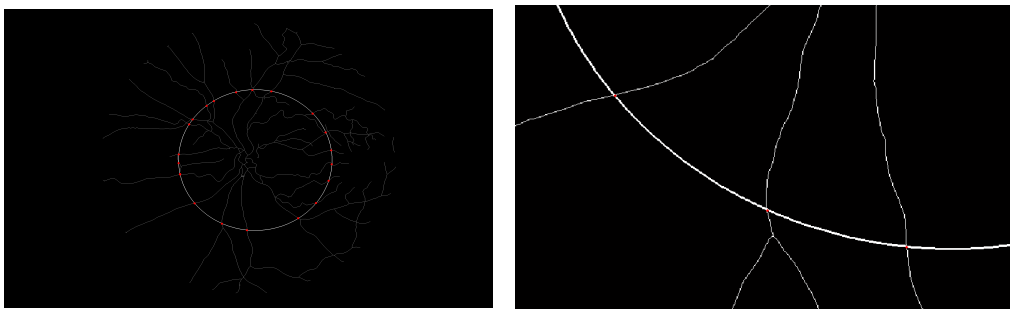

(a) (b)

Figure 3.1: Example of intersections (red dots) between vessel skeletons and a circle, on the binary vessel map extracted by VAMPIRE from an image: (a) locations along a circle, (b) particular.

Vessel maps are extracted using the VAMPIRE automatic package [15] and skeletonisation is performed by the MATLAB *bwmorph* function, based on iterative deletion of pixels and preserving 8-neighbour connectivity.

Widths are estimated automatically using Lupascu et al.'s method [27], described in section 2.1, which basically fits a parametric model of the image's intensity profile across the vessel and then estimate width from the best profile. To minimize accidental errors, each width is computed as the average of the widths at N=9 adjacent locations centred on the target point. Moreover, a location is accepted only if the standard deviation of the 9 measurements was below 10% of the mean.

Information on vessel type is also available: AV classification is performed by a supervised classification and features selection based on Zampierini et al.'s algorithm [31], described in section 2.2. Errors in the automatic results were checked manually to

ensure 100% correct classification.

The two classifiers (vessel diameter estimation and AV classification) were trained on our images to improve the performance.

A total of about 8×10^4 width measurements were collected using the methods above from 136 images.

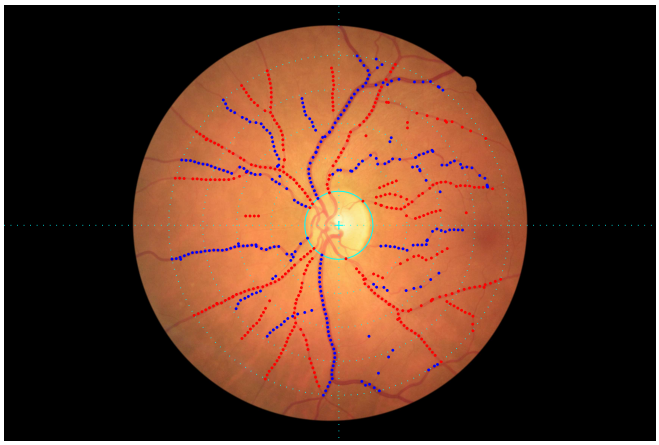

Figure 3.2: Final result of the algorithm after locations detection, width estimation and AV classification.

Data collected can be displayed in Figure 3.3. The 3d histograms were generated by the MATLAB *hist3* function and allow to visualize the frequencies of the combination of levels for two variables, respectively the distance from the OD an the width value in each location. Different plots were generated for arteries and veins.

3.3 Computational time

Width's estimation for a large number of points (order of magnitude 8×10^4) requires a considerable computation time: indeed the algorithm takes several seconds on width's estimation in each intersection, which is estimated as the mean of 9 measurements taken along the vessel. It clearly depends on the CPU and in our experiment we can assume an average time of about 12 s for each intersection. Every image was processed in approximately in 1.30h, for a total the number of 68 images.

Also AV classification requires a computational time not negligible, comparable with the time required for width's estimation. The most is taken by the extraction extraction

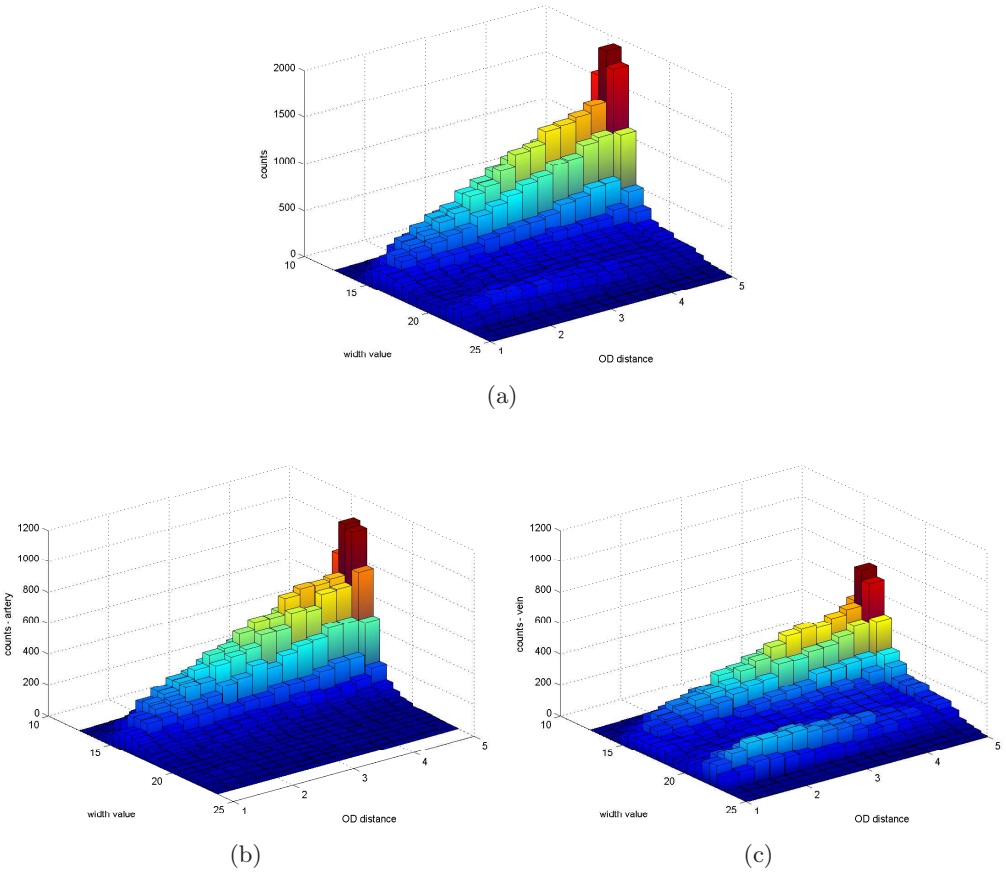

(a)

(b)

(c)

Figure 3.3: Distribution of the widths as a function of OD distance: (a) arteries + veins, (b) arteries, (c) veins.

of the 44 features. Every image was processed in about in 1h.

Vessel diameter's estimation and AV classification were performed in two different runs for organizational set-up reasons. Tests were made on an Intel(R) Core(TM)2 Duo CPU (2.26 GHz) with 3GB RAM memory.

3.3.1 Registration of the images

A preliminary operation of registration of the images was leaded to define coordinates of each location in a new reference system (Figure 3.4): this operation allows the overlapping of the OD centres and of the OD-fovea axis.

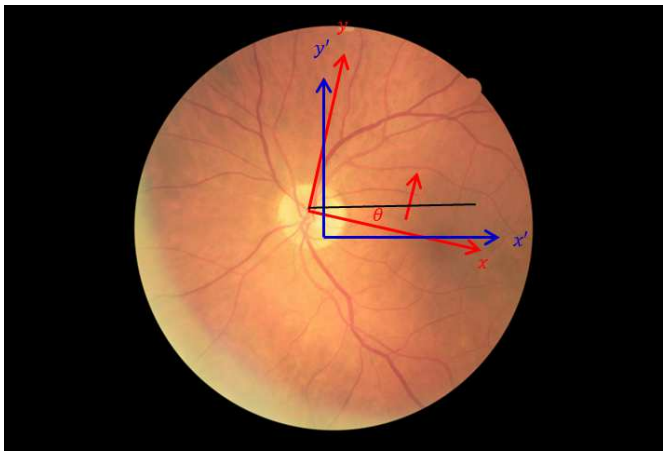

Figure 3.4: Definition of the new reference system x'y' is in blue, the old one xy in red.

Registration is performed by a combination of affine transformations: the Cartesian coordinates of every locations are firstly shifted in the origin of a new reference system and then rotated by an angle θ between the horizontal axis and the line connecting the OD centre with the fovea. The rotation is clockwise or counter-clockwise depending if the eye is left or right. The coordinates of each location are finally scaled to obtain a 200 pixel radius in each image. The transformation can be described by the following matrix form:

$$\begin{bmatrix} x' \\ y' \end{bmatrix} = s \begin{bmatrix} \cos\theta & -\sin\theta \\ \sin\theta & \cos\theta \end{bmatrix} \begin{bmatrix} x \\ y \end{bmatrix} + s \begin{bmatrix} x_0 \\ y_0 \end{bmatrix} \tag{3.1}$$

where x, y are the coordinates of the location in the original reference system and x', y', x_0, y_0, are respectively the coordinates of the location and the OD in the new one ans s is the scaling factor.

3.3.2 Interpolation

Data collected can be stored on a mask of the same size the original images (Figure 3.5), which contains values of every location detected with coordinates in the reference system described in 3.1. If two or more locations have the coordinates we chose the mean value. Thus, we obtain a set of scattered points from which we have to create a continuous surface, using an interpolation method to predict values at every point. It's a similar problem of surface interpolation geo-sciences deal with to estimate data (elevation, temperature, concentrations) from limited observational records.

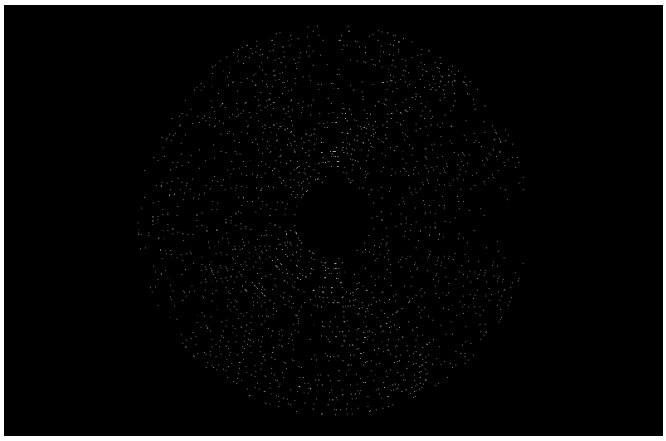

Figure 3.5: Sample set of point locations, after images registration, to be interpolated.

There are two main groupings of interpolation techniques: deterministic and geo-statistical. Deterministic interpolation techniques create surfaces from measured points, based on either the extent of similarity (inverse distance weighted) or the degree of smoothing (radial basis functions). Geo-statistical interpolation techniques (e.g. Kriging) utilize the statistical properties of the measured points. Geo-statistical techniques quantify the spatial autocorrelation among measured points and account for the spatial configuration of the sample points around the prediction location.

We chose the inverse distance method (IDW) because of the sampling sufficiently dense. IDW interpolation explicitly implements the assumption that things that are close to one another are more alike than those that are farther apart. To predict a value for any unmeasured location, IDW uses the measured values surrounding the prediction location. The measured values closest to the prediction location have more influence on the predicted value than those farther away. IDW assumes that each measured point has a local influence that diminishes with distance. It gives greater weights to points closest to the prediction location, and the weights diminish as a function of distance, hence the name inverse distance weighted. In IDW the value $\widehat{z}$ of un-sampled is given

by the following formula:

$$\widehat{z}(x_j) = \sum_{i=1}^{n} \lambda_i z_i \tag{3.2}$$

where λ_i is the weight of the each observation and n the number of the sampling points. Usually the weights are normalized in the range [0 1]:

$$\sum_{i=1}^{n} \lambda_i = 1 \tag{3.3}$$

Weights are proportional to the inverse of the distance between the sample point and the prediction location, raised to the power value p. As a result, as the distance increases, the weights decrease rapidly. The rate at which the weights decrease is dependent on the value of p. Inverse Squared Distance (i.e. p=2) is a widely used interpolator, so the IDW interpolator can be rewritten as follws:

$$\widehat{z}(x_j) = \frac{\sum_{i=1}^{n} z(x_i) d_{i,j}^{-2}}{\sum_{i=1}^{n} d_{i,j}^{-2}} \tag{3.4}$$

The characteristics of an interpolated surface can be controlled by limiting the input points used. Points can be limited by specifying a maximum nunber of points, which will select the nearest points until that maximum number of points is reached. Alternatively, a radius can be specified in maps units (Figure 3.6).

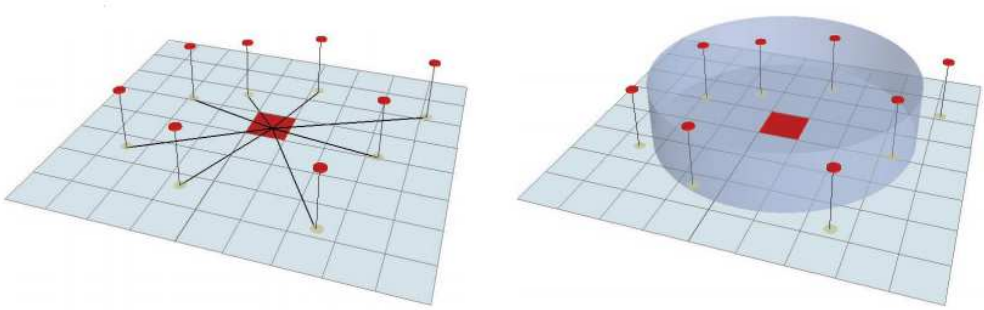

(a) (b)

Figure 3.6: IDW search area: (a) maximum number of neighbours, (b) fixed radius.

We first performed an IDW interpolation on a grid of 288 × 432 nodes, obtained taking 8 pixels far node along rows and columns in the mask of size 2304×3506. A spline

2d-interpolation, performed by the MATLAB function *interp*2, followed to interpolate every pixel of the mask.

3.4 Results

14 images were excluded from the study (8 because of a different scale factor, 6 because too damaged), so the set was reduced to 136 images. Different plots are generated for arteries and veins, left and right eyes.

In Figure 3.7 there are results of widths distribution after the interpolation. Different plots were generated for arteries and veins, for left and right eyes. The maps can be visualized using colour coded images to aid the medical diagnosis.

3.4.1 Cross-validation

Although no measures are known that would or could be universally applied to choose the optimal set of parameters, cross-validation is often used to select an interpolator from finite number of candidates. It is common practice to use k-fold cross-validation method to validate the accuracy of an interpolation when the data set is numerous. The method is based on removing k data points at a time, performing the interpolation for the location of the removed points using the remaining samples and calculating the difference (residual) between the actual value of the removed data point and the estimate for this point obtained from remaining samples. This scenario is repeated k times, with each of the k subsamples used exactly once as the validation data. The overall performance of the interpolator is then evaluated as the root-mean of squared residuals:

$$RMSE = \sqrt{\frac{1}{N}\sum_{i=1}^{N}(z_i - \widehat{z}_i)^2} \tag{3.5}$$

where RMSE stands for root-mean-squared error, z_i is the interpolated value of variable at point i, z_i is the measured value of variable, and N is the number of data points.

Cross-validation was used to find the best agreement between the measured data and the IDW estimates performed with different sets of parameters. The number of closest samples chosen varied from 4 to 16, with a four-sample interval. The best neighbours sample number was found to be 16. We tested only Inverse Square Distance.

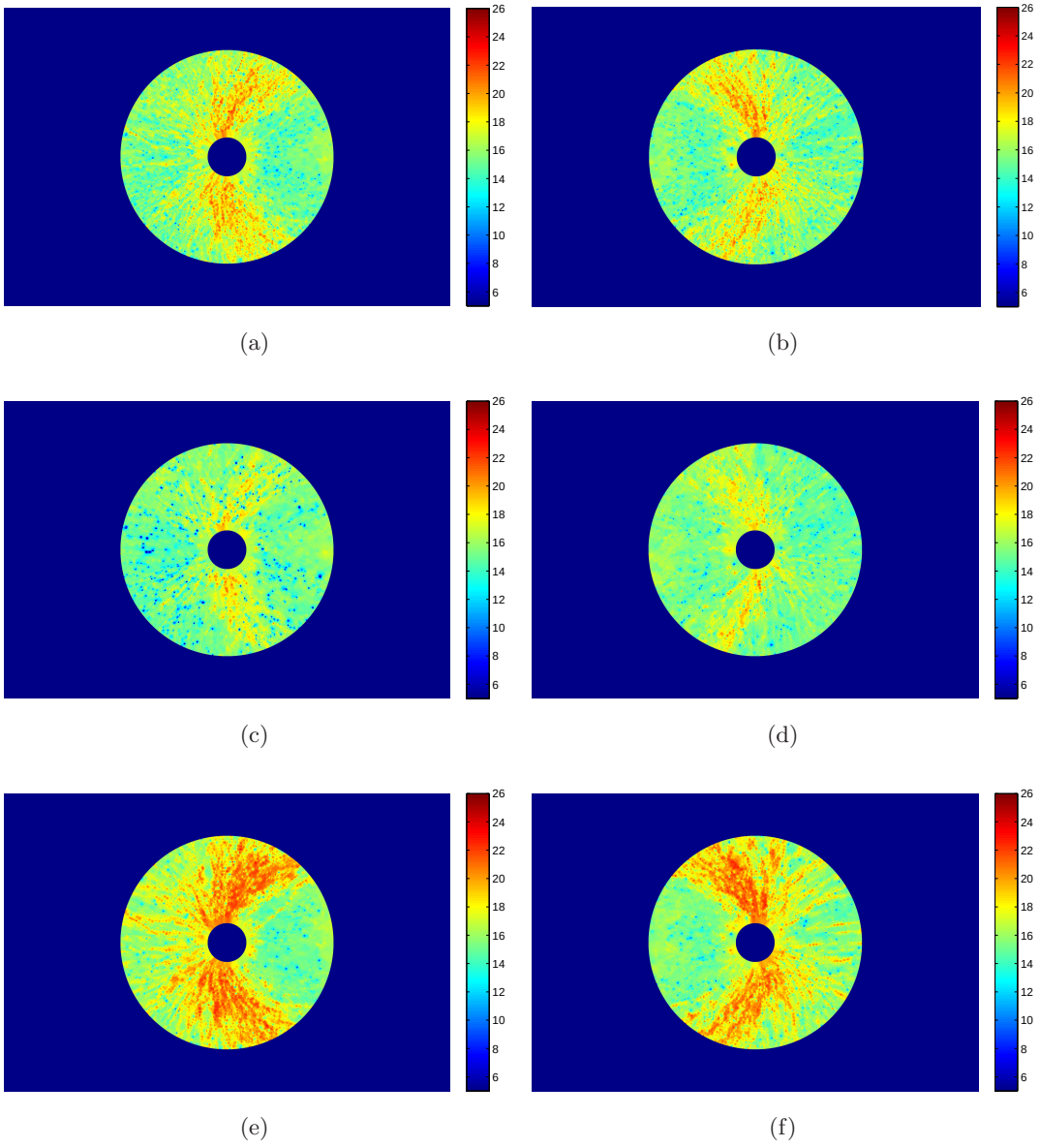

Figure 3.7: Widths distribution map in left and right eye: (a), (b) arteries + veins, (c), (d) arteries, (e), (f) veins.

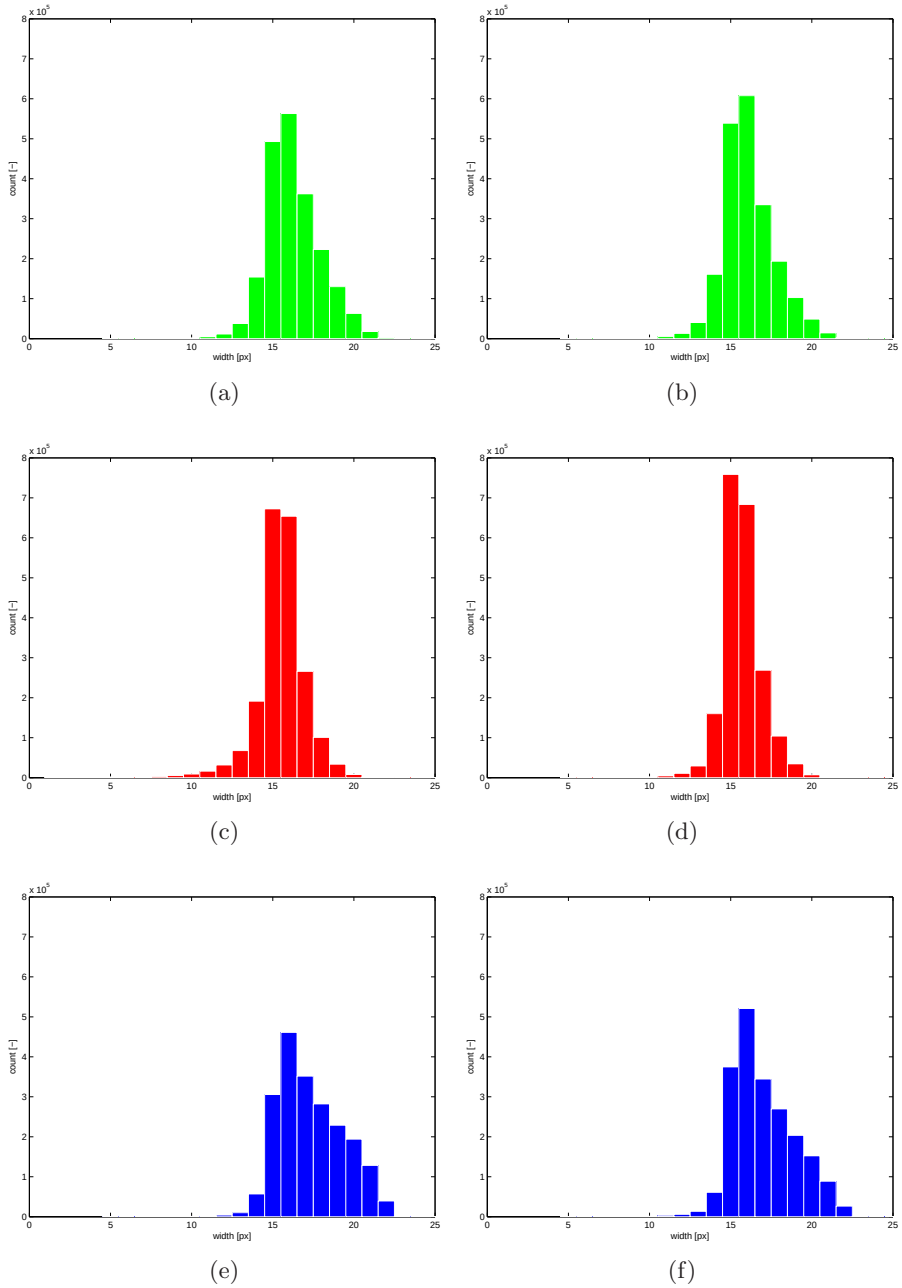

Figure 3.8: Widths distribution histograms for artery + vein (green) artery (red), vein (blue) in left right eye.

3.4.2 Metrics for comparing maps

In the following section we briefly present some measurements that quantitatively evaluate the amount similarity of two images. Two of them come from the images registration theory, the others two are based on the comparison of the grey scale histograms.

Maps of different sub-populations can be compared each others thanks the concepts of mutual information (MI), who represents the amount of similarity of two images. As a similarity measure, mutual information has enjoyed a great deal of success, particularly in the medical imaging domain, and has emerged in recent years as a well-established algorithm in image-registration.

MI between two variables is a concept with roots in information theory and essentially measures the amount of information that one variable contains about another. MI is closely related to joint entropy concepts (H). Specifically, given image X and image Y, the joint entropy $H(X, Y)$ can be calculated as:

$$H(X, Y) = -\sum_{x,y} p(x, y) \log p(x, y) \tag{3.6}$$

where $p(x, y)$ is the joint probability distribution function of pixels associated with images X and Y. The joint probability for each couple is computed from the joint histogram, who displays in x-axis the grey values of the pixels of X and in y-axis those of Y, both considered as realizations of a random variable. The joint entropy is minimized (and the mutual information is maximized) when there is a one-to-one mapping between the pixels in X and their counterparts in Y and it increases as the statistical relationship between X and Y weakens.

Mutual information considers both the joint probability distribution function of X and Y, $p(x, y)$, and the marginal probability distribution function of X and Y, respectively $p(x)$ and $p(y)$. It can be defined as:

$$MI(X, Y) = \sum_{y} \sum_{x} p(x, y) \log \frac{p(x, y)}{p(x)p(y)} \tag{3.7}$$

MI can be equivalent expressed as:

$$MI(X, Y) = H(X) + H(Y) - H(X, Y) \tag{3.8}$$

A frequently used technique in data analysis is the comparison of two distributions

through the comparison of histograms, in terms of some specific criteria for similarity [33], [34]. To compare two histograms H_1 and H_2, first we have to choose a metric $d(H_1, H_2)$ to express how well both histograms match. There are several measurements of similarity [35]: correlation, chi square, intersection, Bhattacharya. E.g. correlation metric can defined as:

$$d(H_1, H_2) = \frac{\sum_i H_1'(i) H_2'(i)}{\sqrt{\sum_i H_1'^2(i) H_2'^2(i)}} \tag{3.9}$$

where:

$$H_k'(i) = H_k(i) - (1/N) \sum_j H_k(j) \tag{3.10}$$

and N equals the number of bins in the histogram. For correlation, a high score represents a better match than a low score. A perfect match is 1 and a maximal mismatch is -1; a value of 0 indicates no correlation (random association).

Chi-square metric (χ^2) comes from is a statistical test for testing the null hypothesis that the distribution of a discrete random variable coincides with a given distribution. It can be express as:

$$d(H_1, H_2) = \sum_i \frac{(H_1(i) - H_2(i))^2}{H_1(i) + H_2(i)} \tag{3.11}$$

For chi-square, a low score represents a better match than a high score. A perfect match is 0 ans a total mismatch is unbounded (depending of the size of the histogram).

3.4.3 Characterization of the community dwelling older population

Using histograms comparison metrics, mutual information and joint entropy concepts, evaluations of sub-population maps were performed, comparing left and right eyes in arteries, veins and total vessel maps. All groups show high correlation. The higher MI has been found in arteries distribution between left and right eye, while veins has the lowest one. The results are displayed in table 3.1.

We performed a further analysis to establish if there were substantial differences between sarcopenic and non-sarcopenic participants. We focused on the arterial maps because it has assumed that arteriolar narrowing is an important risk factor for cardiovascular disease, to which is related sarcopenia disease. Two maps were created from

Groups	MI [*bit*]	H [*bit*]	Corr. [-]	χ^2 [-]
A+V left / A+V right	1.40	2.18	0.96	0.006
A left / A right	1.42	2.03	0.97	0.027
V left / V right	1.36	3.32	0.93	0.014

Table 3.1: MI H, correlation and χ^2 between different groups of population (A = arteries, V = veins).

the 27 participants affected by sarcopenia/pre-sarcopenia and from 27 non-sarcopenic participants. Analysis on the left, right eye, between arteries and veins of the two groups were performed. The same number of participants in the two groups ensures comparability of data. As usual H, MI, correlation and χ^2 were used to compare maps. The following table summarizes the results:

Groups	MI [*bit*]	H [*bit*]	Corr [-].	χ^2 [-]
(A+V) left / (A+V) left	1.44	2.03	0.97	0.005
(A+V) right / (A+V) right	1.40	2.08	0.96	0.018
A left / A left	1.49	1.79	0.97	0.025
A right / A right	1.49	1.78	0.97	0.029
V left / V left	1.41	2.20	0.94	0.008
V right / V right	1.37	2.25	0.94	0.011

Table 3.2: MI, H, correlation and χ^2 between histograms of sarcopenic and non-sarcopenic group (A = arteries, V = veins).

These results show that there are not significant differences between MI and H values in the maps of left and right eye, when comparing the same type of vessels. Maps of veins show the lowest correlation, maps of the arteries the highest. All the groups show similar histograms of widths.

3.5 Discussion

We proposed an innovative population image-based approach to retinal biomarkers, based on the estimation of the distribution of retinal vessel diameter. We analysed lots of fundus camera images of community dwelling older people, collecting a large number of data and testing two classifiers (vessel width estimation and AV classifier). We collected a large number of data, automatically detecting locations at different OD distance and we interpolated data with IDW in order to create a raster surface. We compared maps and found no significant differences between the widths distribution in left and right eye, neither in arteries neither in veins, although the arteries map is

slightly more correlate than the veins one. In saying this, we have to keep in mind some errors the algorithm can commit, i.e. the detection false positive locations because of a bad segmentation, the widths estimation error and the interpolation error. Reducing these errors could modify the results and lead to different maps.

We identified participants affected by sarcopenia (and pre-sarcopenia) and yielded maps for sarcopenic and non-sarcopenic population. We compared the plots of the two healthy in order to verify if the distribution of the widths is different in healthy and patient population. These results show an high correlation between maps of left and right eye, when comparing the same type of vessels. Arteries maps have the highest mutual information value.

Such results lead to the conclusion that widths could not play a key role in detecting people affected by sarcopenia, since there are not differences in with distribution in the two groups. However, a limitation of our study is that it was small and a cross-sectional study in community dwelling older people with poor function. Given that, many of our participants had mobility limitation at baseline, we cannot rule out possible differences between retinal microvascular findings in frailer vs fitter older people. It is possible that associations between retinal vascular measures will be more prominent in people with greater vascular risk and diabetes, especially when looking at longitudinal change in retinal vascular measures.

3.6 Conclusions

Our method aims to produce simple and easy-to-read maps that characterize the distribution of vessel widths in a specific population. Results obtained suggest that vessel widths distribution maps have a good potential as a population image-based approach to retinal biomarkers. Using joint entropy and mutual information concepts, we can compare healthy subjects with patients in order to establish if there is any substantial difference between the two groups in vessel diameter distribution. For the while widths does not seem to play a key role in detecting people affected by sarcopenia, but it would be interesting evaluate more data, comparing more separate classes of subjects.

Chapter 4

Surrogate measurements for vessel generation

In this chapter we develop a method for blood flow rate estimation from morphometric measurements and show how it cloud work as a surrogate measurement for vessel generation, for which there is poor agreement in literature.

Vessel generation can be defined as counting the number of junctions encountered in a vessel tree from OD before hitting this vessel. More specifically, consider the fundus retinal images in figure: we expect to see 4 major vessel supplying the 4 quadrant; CRA and CRV usually splits into superior and inferior as it passes through the disc and then each half (uneven) splits into to cover nasal and temporal retina. We can refer as "0 order" the first split into superior/inferior vessels, and as "1^{st} order" the vessels after the next junction.

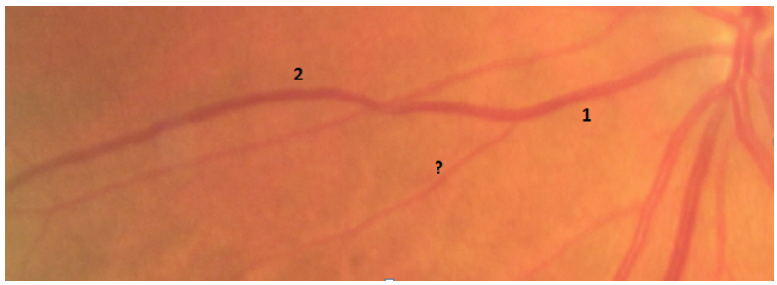

Figure 4.1: The mother vessel branches into 2 daughter vessels with different widths, but we can label for certain the smallest one as "2^{nd} generation".

The main problem is that we can't count every junction as magnitude "order" higher, as some vessels are so small and they clearly do not reduce the size of the mother vessel Figure 4.1. The current thinking is to distinguish junctions from bifurcations, whereby a junction occurs when the daughter vessels have about same width, instead a

bifurcation arise from two daughter vessels with very different widths. When counting to determine generation, ignore bifurcations. A reasonable compromise may be to suggest that junction is of an "order" magnitude if the smallest daughter is above a certain percentage of the width of the parent vessel, although this solution could be arguable and not be acceptable by everyone.

A more scientific approach could be to replace the "generation order" with a surrogate measure related, e.g. with the percentage of the total blood, on a certain distance from OD, carried out on a specific vessel. The same Thus, consider a point P(x,y) on a given vessel; we can call $Q(P)$ the estimated blood flow at P. Trace a circle centered on the OD and passing through P, find all vessels intersecting the circle and sum up all their flows at the points of intersection with the circle; we can call this $\sum Q$. The surrogate measure for generation could be the ratio $Q(P)/(\sum Q)$.

4.1 Materials

We used a set of 150 field-1 retinal images (N=75, left and right-eye images for each) of older people (>65 years, mean age 72 ± 6) volunteers from a recent study on retinal biomarkers for Sarcopenia [5]. Participants with inability to walk independently, past medical history of diabetes mellitus, stroke (within 6 months) and significant visual impairment were excluded from the study. Images were taken at the diabetes screening centre at Ninewells Hospital, Dundee, with a non-mydriatic digital camera after dilation of the pupils with 1% tropicamide eye drops. 13 participants had sarcopenia, 14 had pre-sarcopenia, no one had severe sarcopenia.

4.2 Methods

The alghoritm is organized in 2 main steps, the detection of the locations and the blood flow estimation through the vessel in each location.

A location on a circle is defined as a point where a vessel skeleton crossed the circle and it is detected automatically by an operation of binary intersection of two sets, respectively the skeleton of the binary map of retinal vasculature and a binary circular mask Figure 4.1. Locations are taken at different distance from OD, respectively at 1, 1.5 and 2 ODD (OD distance). Blood flow estimation is computed from vessel diameter and expressed as a percentage of the total flow on a certain distance from OD.

Vessel maps are extracted using the VAMPIRE automatic package [15] and skeletonisation is performed by the MATLAB *bwmorph* function, based on iterative deletion of pixels and preserving 8-neighbour connectivity. Widths were estimated automatically

using Lupascu et al.'s method [27], described in 2.1, which basically fits a parametric model of the image's intensity profile across the vessel and then estimate width from the best profile. To minimize accidental errors, each width was computed as the average of the widths at 9 adjacent locations centred on the target point, and accepted only if the standard deviation of the 9 measurements was below 10% of the mean. Different analysis for arteries and veins are performed; AV classification is carried out by a supervised classification and features selection based on Zamperini et al.'s algorithm [31], described in 2.2.

Furthermore, an interface to correct efficiently by hand wrong locations detected, wrong width estimate and wrong AV labels, due to classifiers errors, is also available.

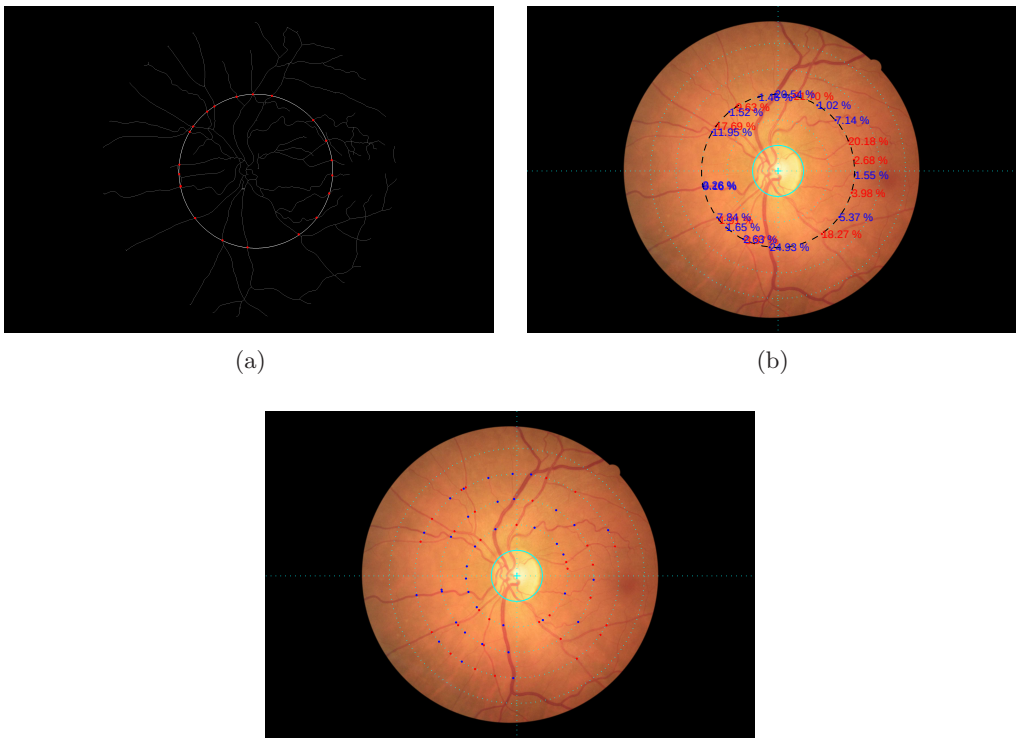

(a) (b)

(c)

Figure 4.2: The main step of the alghoritm: (a) location of intersections, (b) flow's estimation for one circle and (c) AV classification along three circles.

In flow estimation, we considered a Hagen-Poiseuille flow through a pipe: according to the modification of Murray's Law developed by T. Takahashi et. al. [23], we can assume a dependence of blood flow on the $m = 2.85$ power of vessel diameter, $Q = kr^{2.85}$, where Q is the volumetric flow rate, r is the inner radius of the vessel segment and k is a constant.

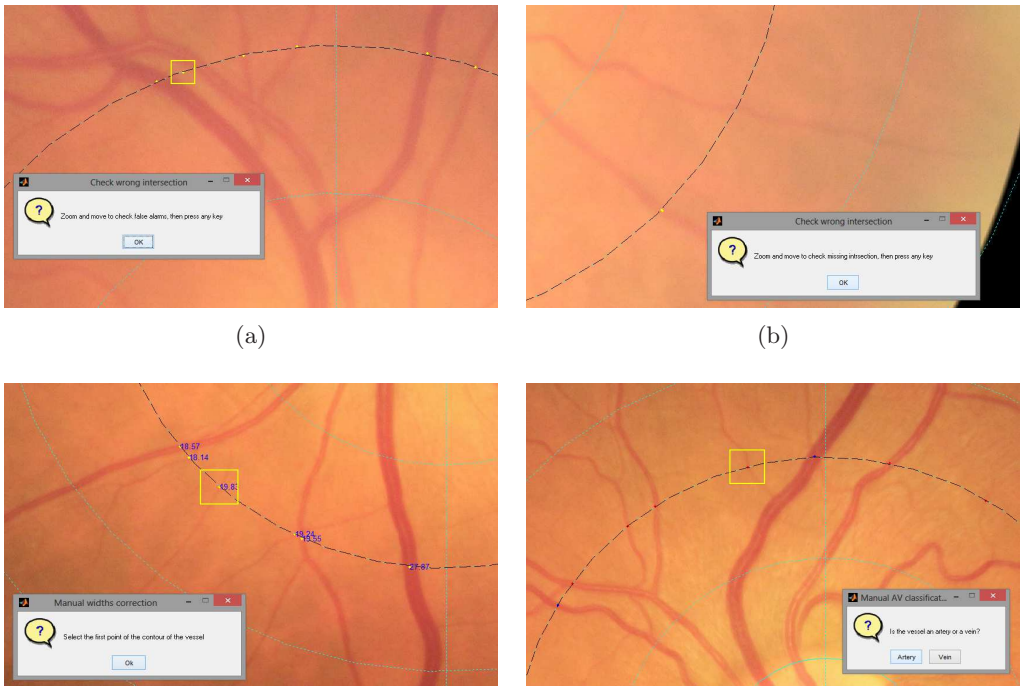

(a) (b)

(c) (d)

Figure 4.3: Tool for manual correction: we can see examples of *(a)* false alamrs, *(b)* missing interections, *(c)* wrong width's diameter estimation and *(d)* wrong AV classification.

We also computed the area of the section pipe, rounding the vessel, according the definition of area of a disk: $A = \pi r^2$ r is the inner radius of the vessel segment. Hence, for a given vessels w_j, flow and area (henceforth Q and A) are computed as a proportion of the flow and area of all vessels intersecting the circle, according to Murray's Law and definition. The following formulae were used:

Flow estimate:

$$Q_j = \frac{w_j^2.85}{\sum_{k=1}^{N} w_k^{2.85}} \tag{4.1}$$

Area estimate:

$$A_j = \frac{w_j^2}{\sum_{k=1}^{N} w_k^2} \tag{4.2}$$

where w_j is the width of the vessel at which the measure is taken, and the sum is taken over the N vessels (including w_j) intersecting the circle (total flow).

For each circle, results were plotted as a function of the angle formed between two axis, the vector from the OD to the location and the vector from OD to the fovea location, counter-clockwise for left eyes, clockwise for right eyes (Figure 4.4).

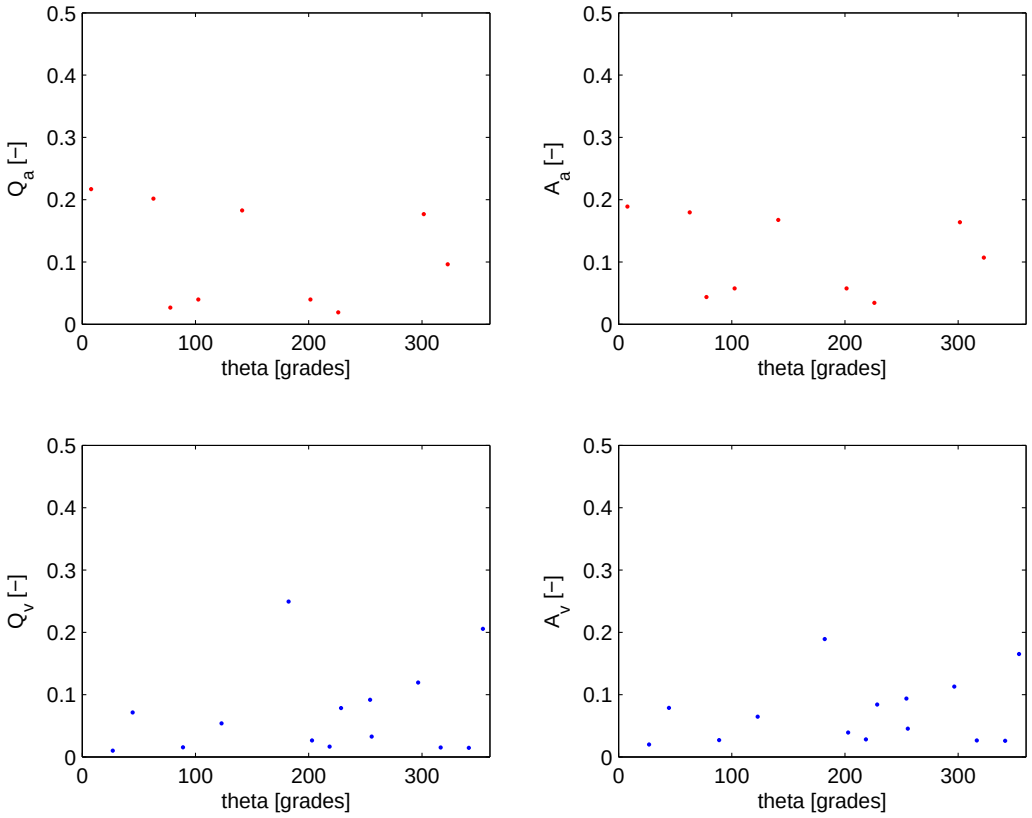

Figure 4.4: Estimated values of flow (Q) and area (A) for arteries (red dots) and veins (blue dots); locations detected at 1.5 ODD.

4.2.1 Equation in retinal miscrovascular network

Despite blood viscosity in miscrovascular network relies on from different parameter, we can consider blood as a Newtonian fluid in first approximation and apply the Hagen-Poiseuille's equation in the flow estimation, derived from Navier-Stokes equation. Specifically, it says that, under the hypothesis of a current of incompressible and Newtonian fluid taking place under conditions of uniform and laminar motion in a rigid circular cylindrical pipe, the volumetric flow rate can be estimated as follows:

$$Q = \frac{\pi \Delta P r^4}{8 \mu L} \tag{4.3}$$

Where, r is the radius of the vessel, $\Delta\ P$ is the pressure drop across the vessel, L is the length of the vessel and μ the blood viscosity. We can highlight the strong dependence of flow on the radius of the tube (fourth power), the pressure gradient over the tube length ($\Delta\ P\ /\ L$ an viscosity of blood (μ). A less detailed and thus more general form of Poiseuille's law is $Q = \Delta\ P\ /\ R$, with resistance R being:

$$R = \frac{8 \mu L}{\pi r^4} \tag{4.4}$$

This law is used in analogy to Ohm's law of electricity, where resistance equals voltage drop/current. The analogy is that voltage difference is compared to pressure drop and current to volume flow. In hemodynamics we also call it Ohm's law. This means that resistance can be calculated from pressure and flow measurements.

Starting from Hagen-Poiseuille's equation, we can derive Murray's Law, who relates the radii of the daughter branches to the radii of the parent branch of a lumen-based system. It assumes that the energy required for blood flow and the energy needed to maintain the vasculature is minimal. The first term equals pressure times flow and, using Poiseuille's law, this is ΔQ. The second term is proportional to the vessel volume and thus equals $b \pi r^2 L$, with b proportionally constant. The total energy E_m is:

$$E_m = \frac{Q^2 8 \mu L}{r^4} + b \pi r^2 L \tag{4.5}$$

The minimal value is found for $\partial E_m / \partial r = 0$ and this lads to:

$$Q = \frac{\pi / 4L}{b / \mu}^{1/2} r^3 = k r^3 \tag{4.6}$$

By the principle of the conservation of mass, the flow of blood in the mother vessel Q_0 must be equal to the sum of the flow of blood through dauthers vessels Q_1 and Q_2:

$$Q_0 = Q_1 + Q_2 \tag{4.7}$$

and thus,

$$r_0^3 = r_1^3 + r_2^3. \tag{4.8}$$

In their paper [23], Takahashi and Nagaoka develop a theoretical and mathematical model to quantitatively describe haemodynamic behaviour in the microvascular network of the human retina. They constructed a symmetric branching network of the human retinal vasculature based on a combination of Murray's law and a mathematical model of fractal vascular trees and supplemented it with physiological and anatomical data available in the literature. The system is characterized by a diameter exponent of $m = 2.85$, instead of 3 as dictated by Murray's law, where the value of $m = 2.85$ is the sum of a fractal dimension (1.70)and a branch exponent (1.15) of the retinal vasculature. This theoretical model allowed to quantitatively assess the hemodynamic parameters, including blood pressure, blood flow, flow velocity, shear rate, and shear stress, as a function of vessel diameter. Thus, in blood flow rate estimation, we can use the following formula:

$$Q = kr^{2.85}. \tag{4.9}$$

This modified formula can also be simply derived from Hagen-Poiseuille's law, when the branch length-radius relationship ($L = 7.4r1.15$) is substituted into Hagen-Poiseuille's law $Q = \frac{\pi \Delta P r^4}{8\mu L}$, so that the final form is $Q = kr^4/r^{1.15} = kr^{2.85}$, where k denotes $(\pi \Delta P)/(7.4 \times 8\mu)$.

4.3 Preliminary results

We performed a preliminary analysis in order to computed the error in blood flow rate estimation. The expected error on Q and A is given by the derivatives of and , e.g., for , after some algebra:

$$\frac{\partial Q_j}{dw_j} = \frac{3w_j^{1.85}}{\sum_{k=1}^{N} w_k^{2.85}} \left[\frac{1 - w_j^{2.85}}{\sum_{k=1}^{N} w_k^{2.85}} \right] \tag{4.10}$$

We have expectations of the width estimation error, ∂w_j, from extensive experiments with Hermite model's method (reported [27]) and the widths are estimated from the images. Hence we can expect the magnitude of the error on Q (A). The expected

error on the relative formula for Q (4.10) increase monotonically with widths and even small variations in width estimate may yield important variations of Q, so we can not take Q (A) as reliable estimates. E.g. in Figure 4.5 are reported 2 plots of ∂Q (on the left) and ∂A (on the right) as functions of the width of the vessels. The widths of the vessels range from 9 to 20 px and for each we can compute the expectation of the magnitude on Q error. For the largest vessel i we have an error $\partial Q/Q_i \approx 0.3$; the smallest one j yield an error of even $\partial A/A_i \approx 0.8$.

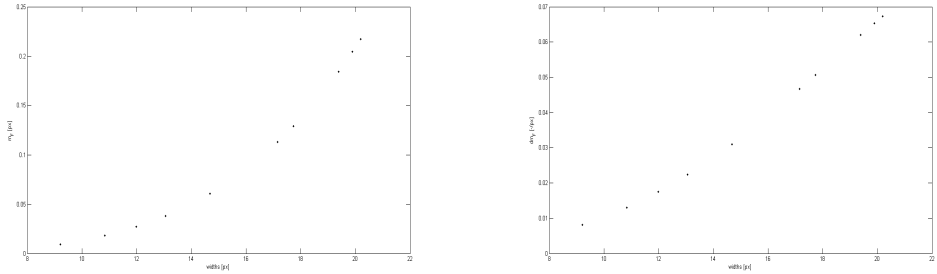

(a) (b)

Figure 4.5: Expected error in: (a) Q estimation and (b) A estimation.

A second issue is related to the formula 4.3, which simplifies excessively the flow rate estimation. Indeed, we considered the term $k = (\pi \Delta P)/(7.4 \times 8\mu)$ constant for all the vessels (indeed equation was obtained by gathering k in the denominator, then dividing numerator and denominator by k); however k contains elements that can be different for different vessels:

- the pressure differential
- the vessel length
- the viscosity coefficient

These cannot be ignored and are probably instrumental for the hypothesized flow balance. Thus, we can conclude that the flow, except for a constant term, is not only function of widths and some others variables have to come into play: firstly, the difference of pressure along the vessel and the viscosity coefficient, which depends on the vessel diameter (F$\circ a$hraeus-Lindqvist effect), flow rate and hematocrit in miscrovascular network. Specifically, blood cannot be treated as homogeneous when flowing within the vessels of the capillary network, whose average diameter is the same order of magnitude as red blood cells in diameter.

Some observations on a few images support the thesis that equation leads to wrong measurements of blood vessel flow rate, e.g. the hypothesis of conservation of flow may

not be verified. Indeed, as shown in Figure 4.6, at several vessel branches, the width of the mother vessel and of one daughter vessel are practically the same, but the width of the second daughter vessel is significant. However, according to the continuity equation, the volume flow splits into two parts: the most one carried on the larger daughter vessel and a minor one carried the smaller one; but computing with the simplified formula , the mother vessel and the larger daughter one look like to bring the same flow volume.

Figure 4.6: The mother vessel branches into 2 daughter vessels: the diameter of the left daughter vessel looks like the same or even bigger than the one of parent vessel.

This results presented in the previous section lead to the conclusion that the computing of the flow in microcirculation, as the retinal circulation is, can't be just simply, with the Murray's law. Thus, the blood flow can't be reduced as function of just vessel diameter and local morphological features per se do not allow to calculate flow, since they give no information on local pressure drop and viscosity. Indeed, heterogeneity is a hallmark of microvascular networks and parameters usually exhibit large coefficients of variation. Thus, flow would have to measured independently, e.g. from time time series images (e.g. fluorescein angiogram) or from laser doppler or speckle tracing.

For this reason, we decided to suspend the study and do not perform further analysis.

4.4 Conclusion

We developed a new definition of a surrogate measurement for vessel generation, based on blood flow rate estimation, for which there is pour agreement in literature. We estimated the blood flow as a function of the vessel diameter, according to a modification of Murray's law, developed in [23]. Unfortunaley, the used formulae haven't yielded to

reliable estimations, since the framework of the vasculature network, at least in our images dataset, does not obey to the Murray's Law and can't be simplified as just a function of vessel diameter. In the future, it would be interesting to compute blood flow with other techniques (e.g the laser doppler) and verify if there is any significant change in blood vessel flow rate in sarcopenic population.

Appendix A

MATLAB code

In the next section we describe, in details, the MATLAB code that performs the estimation of widths distribution, described in Chapter 3.

main.m: detects N=600 locations for each images between vessel skeleton circle mask with different diameters. The algorithm starts the detection of the points in 5 starting circles and continues to add points until the number N is reached. In the first iteration, circles with radii $1, 2, ..., 5$ OD distance (ODD) has been chosen; the radii of the circles in the following iterations are set in the way to drop in the middle of two consecutive circles of the previous one; thus, i.e., for the second iteration $r_i = 1.5, 2.5, ..., 4.5$ ODD.

```
%add circles until nTot >= nBorderMin
while n<nBorder(1)

                kk=length(1+(step/2):step:5-(step/2)); %last kk circles index
                d=[d,1+(step/2):step:5-(step/2)]; %radii's vauue array

                for i=1+nOfCircles:length(d)
                                %find intersection
                                circle(i)=circle_info(datavampire,d(i));
                                %update number of total intersection
                                n=n+circle(i).nInterSection;
                end
                step=step/2; %update sampleRate
                nOfCircles=length(d);

end
```

If the number of the intersections exceeds the limit number N, locations detected in the last iteration are subsampled in order to return within N.

circle.m: perform an automatic width's estimation, and AV classification of retinal vessels at locations detected by the function *intersection.m*. Results are stored in the structure *circle*, which provides informations about locations detected: distance from the OD, polar and Cartesian coordinates of the location, vessel diameter and type of vessel.

Cartesian co-ordinate are defined by a spatial reference system with orign on the top left corner of each image and axis oriented as follows: x-axis from the left to the right the horiziontal axis, y-axis from the top to the bottom the vertical one. Polar co-ordinates, instead, have been adjusted to allow in order to be related to the morphometric features of the retina (fovea and OD). The origin of the reference system is the OD centre; the angular coordinate, instead, starts from the orthogonal to the line connecting the OD centre with the fovea and has opposite direction for left (clockwise) and right (counterclockwise) eye Figure A.1. In this way the two eyes have a reference system symmetrical to the sagittal plane and the corresponding structures in the left and right retina have the same coordinates.

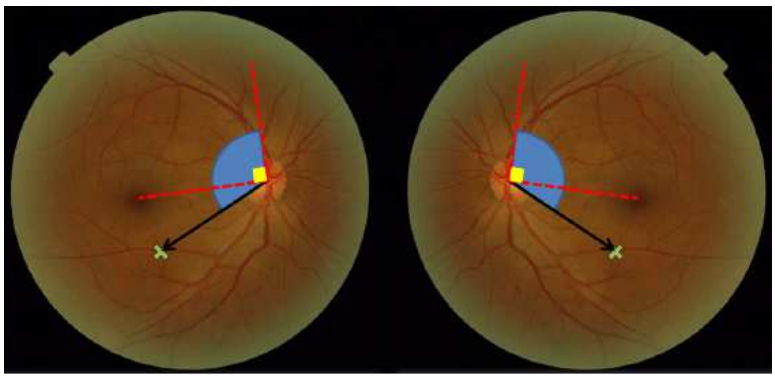

Figure A.1: Polar coordinates of a point of interest (green cross): the black arrow represents the linear coordinate, in blue the angular coordinate with respect to the reference axis (in red).

intersection.m: location of intersections of vessels with circles centred on OD of arbitrary diameter d. The detection of the points is achieved by an operation of binary intersection of two sets, respectively the skeleton of the binary map of retinal vasculature, provided from VAMPIRE tool, and a binary circlular mask.

```
%find intersection between mask & skel
intersection=(skel & mask);
[r,c]=find(intersection==true);
```

Skeletonisation of the vasculature map is performed by the MATLAB *bwmorph* function, based on iterative deletion of pixels and preserving 8-neighbour connectivity: the result is an image in which each blood vessel is one pixel thick. A one pixel thin circular mask is built setting the coordinates rounding the circumference to a *true* value.

```
%draw circles
deg=0:0.001:1; %degree

%circle's coordinates
x=x_OD+radius*cos(2*pi*deg)*d;
y=y_OD+radius*sin(2*pi*deg)*d;

%create circle's mask
mask=false(size(skel));
for i=1:length(x)
    mask(uint16(y(i)),uint16(x(i)))=true;
end
```

Morphological operations (dilation following by thinning) are then applied in order to obtain a connected two-pixel boundaries mask.

```
%connect mask's pixel
mask=imdilate(mask,strel('diamond',10));
mask=bwmorph(mask,'thin',Inf);
%2 px mask's width to intersect all the vessels
mask=imdilate(mask,strel('diamond',1));
```

In this way we can detect all the vessel: indeed some vessels would over-cross without intersect a one pixel thin mask. False positive are detected too (Figure B.2), thus, only intersections more than three pixel far (chessboard distance) from each others are considered corrected intersection points.

```
dist=[];
%delete false intersection
for i=1:length(r)-1
    %chessboard distance
    dist(i)=max(abs(c(i)-c(i+1)),abs(r(i)-r(i+1)));
end

dist(i+1)=max(abs(c(end)-c(1)),abs(r(end)-r(1)));
indx=find(dist>=3);

r=r(indx);
c=c(indx);
```

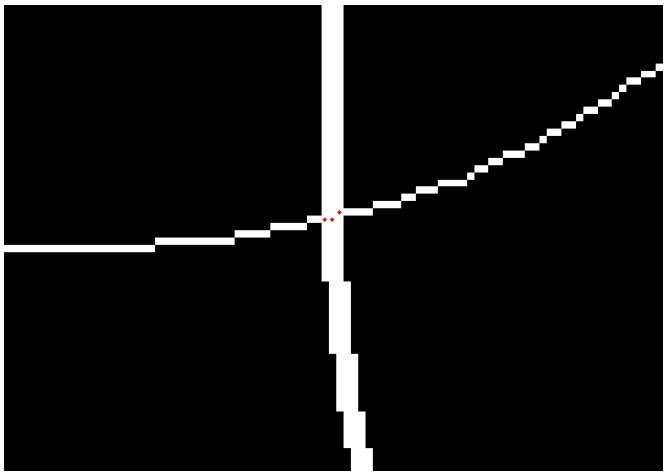

Figure A.2: False positive (red dots) detected by the intersection between the skeleton mask and the 2 pixel circular mask.

HermiteAroundPoint.m: estimates, for each location, vessel diameter as the average of the widths at N = 9 adjacent locations centred on the target point. In each location estimation, we don't consider measurements out of range of the 10 and 90 percentiles of the 9 widths computed. Moreover, a location is accepted only if the standard deviation of the 9 measurements was below 10% of the mean. The tracking the vessel is based on gradient orientation analysis: the orientation of a vessel in $P(x, y)$ is computed from the numerical gradient $[\partial x \partial y]$ in a window centred in P, eigenvectors are calculated by svd (singular value decomposition) analysis and the normalized values are assumed as the main direction of the vessel in P.

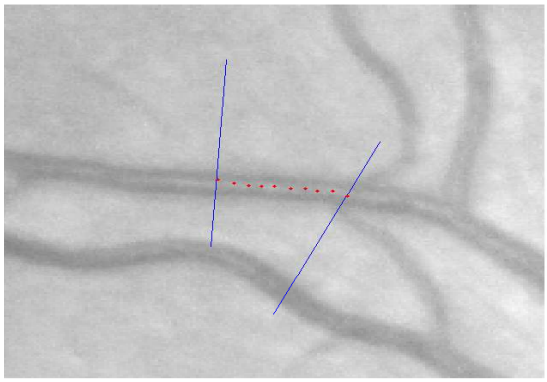

Figure A.3: Tracking of the vessel.

Appendix B

Training of the classifiers

In order to improve classifiers accuracy, we trained them on sarcopenic images dataset. The set includes of 138 fundus images, both OD centred and macula centred, resolution 2304×3504, provided by Ninewells Hospital, Dundee, and obtained in full conformity with the current protocols (ethics, Caldicott, anonymization). In the following section we report of the new training.

B.1 Width estimation

Regarding vessel diameter's estimation, two observers (final year Biomedical Engineering students) estimated widths for 362 cross-sections of main and secondary vessels, both veins and arteries, with a purpose-designed graphical interface allowing vessel magnification and pixel selection. The mean of the two manual measurements wass used as the gold standard (third observer).

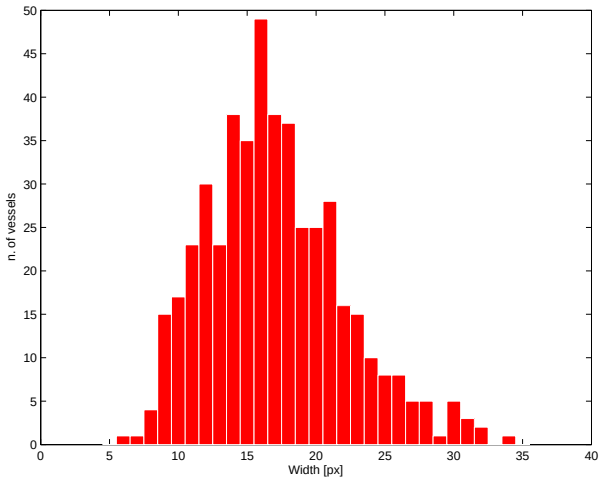

Figure B.1: Distribution of number of samples per width in the dataset.

K-fold cross validation ($K = 10$) was performed in order to estimate the accuracy of the predictive model. Prediction error was computed as the mean and standard deviation of the differences between the estimation of the model and the ground truth; so for the i-th profile, we can write the classification error χ_i as follows:

$$\chi_i = \omega_i - \varphi_i \tag{B.1}$$

where ω_i is the estimated width and φ_i is the ground truth of the i^{th} profile. We obtained an error of 1.8 ± 1.2 px, consistent with the results obtained in [27].

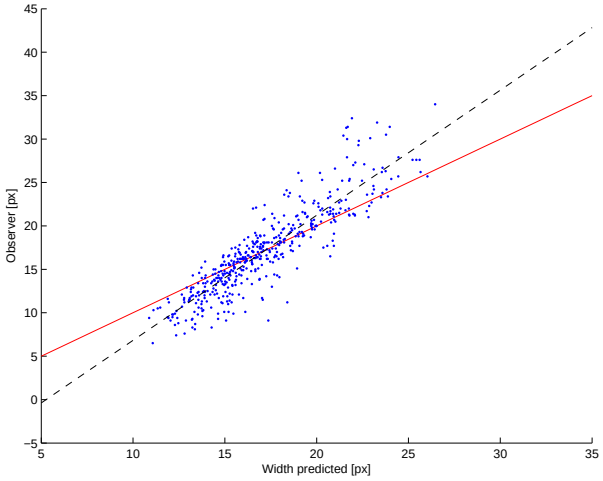

Figure B.2: Correlation between classify's predictions and ground truth.

Figure B.2 shows the correlation of predicted vessel widths and the observer's measurements: the regression line shows the prediction tends to underestimate large vessels and to to overestimate the narrow vessels, compared to the observers's measurements.

B.2 AV classification

The same dataset was used to train the AV classify: it consists of vessels of different size, half arteries and half veins, labelled by a final year Bomedical Enginering student. In order to exploit maximally the available data, without creating biased results, we performed classification procedures with a leave-image-out protocol, i.e. averaging results obtained by taking test points on one image and training points on all the other in the dataset. Despite the results obtained in [31], the best accuracy was provided by Support Vector Machine classifier, with a subset of 44 features and a subsampling resolution factor of 0.625, comparable with the classification error obtained in [31].

Conclusion

In this study we analyzed lots of fundus camera images of a community dwelling older people in order to look for retinal biomarkers for sarcopenia.

We proposed an innovative population image-based approach to retinal biomarkers, based on the estimation of the distribution of retinal vessel diameter. Our method aims to produce simple and easy-to-read maps that characterize the distribution of vessel widths in a specific population. We collected a large number of data, automatically detecting locations at different OD distance and testing two classifier for widths estimation and AV classification. We interpolated data with IDW in order to create a raster surface. Using mutual information and joint entropy concepts, we compared maps of sarcopenic and non-sarcopenic population looking for any difference between the two class. High correlation was found in each comparison, both in veins and arteries, both in left and right eye. Thus vessel diameter seem not to play a crucial role in detecting people affected by sarcopenia, since there is no significant change in vessel widths. However, it would be interesting evaluate more data, comparing more separate classes of subjects.

We developed a new definition of a surrogate measurement for vessel generation, based on blood flow rate estimation, for which there is pour agreement in literature. We estimated the blood flow as a function of the vessel diameter, according to a modification of Murray's law. The used formulae haven't yielded to reliable estimations, since the framework of the vasculature network, at least in our images dataset, does not obey to the Murray's Law and can't be simplified as just a function of vessel diameter. In the future, it would be interesting to compute blood flow with other techniques and verify if there is any significant change in blood vessel flow rate in sarcopenic population.

Bibliography

[1] C. Chiu, H. Weber, S. Adamski, A. Rauch, G. M. A., S. E. Alves, G. Kath, O. Flores, and H. A. Wilkinson, "Non-invasive muscle contraction assay to study rodent models of sarcopenia." *BMC Musculoskelet Disord*, 2011.

[2] P. Clayton, "Sidestepping sarcopenia: Avoiding the loss of muscle mass." *Gencor, Lifestyle Solutiona*, 2013.

[3] D. Sumukadas, "Retinal microvascular properties as biomarkers for sarcopenia: a pilot study." *TENOVUS*, 2011.

[4] I. Janssen, D. Shepard, P. Katzmarzyk, and R. Roubenoff, "The healthcare costs of sarcopenia in the united states." *Journal of the American Geriatrics Society.*, pp. 80–85, 2004.

[5] "Does the european working group on sarcopenia in older people algorithm detect all those vulnerable?" University of Dundee - 2013.

[6] G. Mitchell, H. Parise, E. Benjamin, L. M.G., M. Keyes, and J. Vita, "Changes in arterial stiffness and wave reflection with advancing age in healthy men and women: the framingham heart study." *Hypertension*, pp. 1239–1245, 2004.

[7] M. Ochi, K. Kohara, Y. Tabara, T. Kido, E. Uetani, and N. Ochi, "Arterial stiffness is associated with low thigh muscle mass in middle-aged to elderly men." *Atherosclerosis*, pp. 327–332, 2012.

[8] V. Katsi, C. Vlachopoulos, G. Souretis, K. Baou, I. Dagalaki, and N. Alexopoulos, "Association between retinal microcirculation and aortic stiffness in hypertensive patients." *Int.J Cardiol.*, 2011.

[9] N. Cheung, A. Sharrett, R. Klein, M. Criqui, F. Islam, and K. Macura, "Aortic distensibility and retinal arteriolar narrowing: the multi-ethnic study of atherosclerosis." *Hypertension*, pp. 617–622, 2007.

[10] R. Snell, *Clinical Anatomy by Regions, Ninth Edition.*, 2012.

[11] H. Kolb. (2011) Webvision - simple anatomy of the retina. [Online]. Available: http://webvision.med.utah.edu/book/part-i-foundations/simple-anatomy-of-the-retina/

[12] N. Patton, T. Aslam, T. MacGillivray, I. Deary, B. Dhillon, R. Eikelboom, K. Yogesan, and I. Constable, "Retinal image analysis: concepts, applications and potential." *Progress in Retinal and Eye Research*, pp. 99–127, 2006.

[13] E. Trucco, A. Ruggeri, T. Karnowski, L. Giancarlo, E. Chaum, J. P. Hubschman, B. Al-Diri, C. Y. Cheung, D. Wong, M. Abramoff, G. Lim, D. Kumar, P. Burlina, N. M. Bressler, H. Jelinek, F. Maiaudeau, G. Quellec, T. MacGillivray, and B. Dhillon, "Validating retinal fundus image analysis algorithms: Issues and a proposal." *Investigative Ophthalmology and Visual Science*, pp. 3546–3559, 2013. [Online]. Available: papers/TruccoIOVS2013.pdf

[14] A. Perez-Rovira, T. MacGillivray, E. Trucco, K. Chin, K. Zutis, C. Lupascu, D. Tegolo, A. Giachetti, P. Wilson, A. Doney, and B. Dhillon, "Vampire: Vessel assessment and measurement platform for images of the retina." in *Proceedings of the Biosignals and Biorobotics Conference (BRC)*, 2011, pp. 3391 – 3394.

[15] E. Trucco, L. Ballerini, D. Relan, A. Giachetti, T. MacGillivray, K. Zutis, C. Lupascu, D. Tegolo, E. Pellegrini, G. Robertson, P. Wilson, A. Doney, and B. Dhillon, "Novel vampire algorithms for quantitative analysis of the retinal vasculature." in *Proceedings of the IEEE International Conference*, 2013.

[16] A. Giachetti, K. Chin, E. Trucco, C. Cobb, and P. Wilson, "Multiresolution localization and segmentation of the optical disc in fundus images using inpainted background and vessel information," *ICIP*, pp. 2145–2148, 2011.

[17] G. Loy and A. Zelinsky, "Fast radial symmetry for detecting points of interest." *IEEE Trans*, pp. 959–973, 2003.

[18] J. Soares, J. Leandro, R. Cesar, H. Jelinek, and M. Cree, "Retinal vessel segmentation using the 2-d gabor wavelet and supervised classification." *IEEE Trans on Medical Imaging, vol 25*, pp. 1214–1222, 2006.

[19] D. Tegolo, C. Lupascu, and E. Trucco, "Fabc: Retinal vessel segmentation using adaboost." *IEEE Trans on Inf. Tech. in Biomedicine, vol 14*, pp. 1267–1274, 2010.

[20] A. Cavinato, "Spline-based refiniment of coutours in binary maps of retinal vessels." 2012.

[21] E. Trucco and B. Azegrouz, H. an Dhillon, "Modeling the tortuosity of retinal vessels: does calibre play a role?" *IEEE Trans. on Biom. Engin.*, pp. 2239–2247, 2010.

[22] R. C.E., "Blood velocity and volumetric flow rate in human retinal vessels." *Investigative Ophthalmology and Visual Science*, pp. 1124–1132, 1985.

[23] T. Takahashi, T. Nagaoka, H. Yanagida, T. Saitoh, A. Kamiya, T. Hein, L. Kuo, and A. Yoshida, "A mathematical model for the distribution of hemodynamic parameters in the human retinal microvascular network." *Japanese Society of Biorheology*, pp. 77–86, 2009.

[24] M. Olufsen, C. Peskin, W. Kim, E. Pederson, and J. Nadim, A.and Larsen, "Numerical simulation and experimental validation of blood flow in arteries with structured-tree outflow conditions." *Annals of Biomedical Engineering*, pp. 281–1299, 2000.

[25] J. Malek, B. Nasralli, F. Echouchene, and R. Tourki, "Geometric and hemodynamic study in early stages of diabetic retinopathy." in *International Conference on Control, Engineering and Information Technology*, 2013, pp. 69–76.

[26] A. Pries, T. Secomb, G. P., and J. Gross, "Blood flow in microvascular networks. experiments and simulation." *Circulation research*, vol. 67, pp. 826–834, oct 1990.

[27] L. C. A., D. Tegolo, and T. E., "Ensembles of bagged decision trees for measuring retinal vessels using an extended multiresolution hermite model." *Progress in Retinal and Eye Research*, 2013.

[28] L. Wang, A. Bhalerao, and R. Wilson, "Analysis of retinal vasculature using a multiresolution hermite model." *IEEE Transactions on Medical Imaging*, 2007.

[29] D. Relan, T. MacGillivray, L. Ballerini, and E. Trucco, "Retinal vessel classification: sorting arteries and veins." in *International Conference on Engineering in Medicine and Biology (EMBC), Osaka (In Press)*, 2013. [Online]. Available: papers/Relan2013.pdf

[30] E. Grisan and A. Ruggeri, "A divide et impera strategy for automatic classification of retinal vessels into arteries and veins." *IEEE Transactions on Medical Imaging*, September 2003.

[31] A. Zamperini, A. Giachetti, E. Trucco, and K. S. Chin, "Effective features for artery-vein classification in digital fundus images." in *25th IEEE International Symposium on Computer-Based Medical Systems (CBMS)*, 2012.

[32] F. Van der Heijden, R. Duin, D. De Ridder, and D. Tax, "Classification, parameter estimation and state estimation: An engineering approach using matlab." *Wiley, 1 edition*, November 2004.

[33] M. Swain and D. Ballard, "Indexing via colour histogram." *International conference on Computer Vision (ICCV).*, pp. 390–393, 1990.

[34] B. Schiele and J. Crowley, "Probabilistic object recognition using multi dimensional receptive field histograms." *ECCV*, pp. 610–619, 1996.

[35] G. Bradski and A. Kaehler, *Learning OpenCV.*, 2008.